

## Mid-InfraRed Outburst in Nearby Galaxies (MIRONG) I: Sample Selection and Characterization

NING JIANG <sup>1,2</sup> TINGGUI WANG <sup>1,2</sup> LIMING DOU <sup>3</sup> XINWEN SHU <sup>4</sup> XUEYANG HU,<sup>1,2</sup> HUI LIU,<sup>1,2</sup> YIBO WANG,<sup>1,2</sup>  
LIN YAN <sup>5</sup> ZHENFENG SHENG <sup>1,2</sup> CHENWEI YANG <sup>6</sup> LUMING SUN <sup>1,2,4</sup> AND HONGYAN ZHOU <sup>1,6</sup>

<sup>1</sup>CAS Key laboratory for Research in Galaxies and Cosmology, Department of Astronomy, University of Science and Technology of China, Hefei, 230026, China; jnac@ustc.edu.cn

<sup>2</sup>School of Astronomy and Space Sciences, University of Science and Technology of China, Hefei, 230026, China; twang@ustc.edu.cn

<sup>3</sup>Department of Astronomy, Guangzhou University, Guangzhou 510006, China; doulm@gzhu.edu.cn

<sup>4</sup>Department of Physics, Anhui Normal University, Wuhu, Anhui, 241000, People's Republic of China

<sup>5</sup> Caltech Optical Observatories, California Institute of Technology, Pasadena, CA 91125, USA

<sup>6</sup>Polar Research Institute of China, 451 Jinqiao Road, Shanghai, 200136, People's Republic of China

### ABSTRACT

The optical time-domain astronomy has grown rapidly in the past decade but the dynamic infrared sky is rarely explored. Aiming to construct a sample of mid-infrared outburst in nearby galaxies (MIRONG), we have conducted a systematical search of low-redshift ( $z < 0.35$ ) SDSS spectroscopic galaxies that have experienced recent MIR flares using their *Wide-field Infrared Survey Explorer (WISE)* light curves. A total of 137 galaxies have been selected by requiring a brightening amplitude of 0.5 magnitude in at least one *WISE* band with respect to their quiescent phases. Only a small fraction (10.9%) has corresponding optical flares. Except for the four supernova (SNe) in our sample, the MIR luminosity of remaining sources ( $L_{4.6\mu\text{m}} > 10^{42}$  erg s<sup>-1</sup>) are markedly brighter than known SNe and their physical locations are very close to the galactic center (median  $< 0''.1$ ). Only four galaxies are radio-loud indicating synchrotron radiation from relativistic jets could contribute MIR variability. We propose that these MIR outburst are dominated by the dust echoes of transient accretion onto supermassive black holes, such as tidal disruption events (TDEs) and turn-on (changing-look) AGNs. Moreover, the inferred peak MIR luminosity function is generally consistent with the X-ray and optical TDEs at high end albeit with large uncertainties. Our results suggest that a large population of transients have been overlooked by optical surveys, probably due to dust obscuration or intrinsically optical weakness. Thus, a search in the infrared band is crucial for us to obtain a panoramic picture of nuclear outburst. The multiwavelength follow-up observations of the MIRONG sample are in progress and will be presented in a series of subsequent papers.

**Keywords:** galaxies: sample — galaxies: active — galaxies: nuclei

### 1. INTRODUCTION

Time-domain astronomy has developed rapidly in the past two decades. The great progress has been driven by the advent of new instruments and facilities dedicated to wide-field, deep and fast surveys, such as Catalina Real-Time Survey (CRTS; Drake et al. 2009), Palomar Transient Factory (PTF/iPTF; Law et al. 2009), Panoramic Survey Telescope and Rapid Response System (Pan-STARRS or PS; Kaiser et al. 2004; Chambers et al. 2016), All Sky Automated Survey for SuperNovae (ASASSN; Shappee et al. 2014), the Asteroid Terrestrial-impact Last Alert System (ATLAS; Tonry et al. 2018) and Zwicky Transient Facility (ZTF; Graham et

al. 2019). These remarkable projects have gradually make it possible to image the entire sky every a few days and process the data in real time. It is believed that LSST will produce an unprecedented time-domain survey in the 2020s.

Supernova (SNe) are absolutely the major class of extragalactic transients and its number has experienced explosive growth as expected with aid of those above-mentioned surveys. In 2018, there were more than 7,000 reported supernovae<sup>1</sup> although most have not been spectroscopically confirmed. In addition to increasing in number of SNe, these surveys have also accelerated the discovery and in-depth studies of peculiar SNe, such as superluminous supernova (SLSNe; e.g., ASASSN-15lh, Dong et al. 2016; see Gal-Yam

Corresponding author: Ning Jiang  
jnac@ustc.edu.cn

<sup>1</sup> <http://rochesterastronomy.org/sn2018/index.html>

2019 as a recent review), exotic SNe with multiple peaks (e.g., iPTF14hls, [Arcavi et al. 2017](#)) and even gravitationally lensed SNe (iPTF16geu, [Goobar et al. 2017](#)). These unusual events could make great breakthrough in our understanding of stellar explosion in extreme physical condition.

The other population of extragalactic variable sources which has aroused great attention is the transient events associated with the supermassive black holes (SMBHs) located in the centers of galaxies. Among them, the tidal disruption event (TDE), in which a star is torn apart by a SMBH's tidal force, is of particular interest. During the process, about half of the stellar mass may be ejected while the rest of the stellar material is accreted on to the black hole, producing a luminous flare of electromagnetic radiation lasting for months to years ([Rees 1988](#); [Evans & Kochanek 1989](#); [Phinney 1989](#)). TDE discoveries require modern time-domain surveys because their event rate is hundreds of times lower than SNe with a rate of  $10^{-4} - 10^{-5}$ /galaxy/year ([Wang & Merritt 2004](#); [Stone & Metzger 2016](#)). Hence, the number of TDEs (or candidates) found to date is still very limited. As a rare and special form of accretion, TDEs are nevertheless extremely scientifically valuable as they offer us an ideal chance to probe the existence, mass and spin of SMBHs in normal galaxies ([Lu et al. 2017](#); [Mockler et al. 2019](#); [Pasham et al. 2019](#)). Moreover, they can serve as a unique laboratory to study the dynamic process of BH activity by witnessing the ignition and flameout of the accretion disk (e.g., [Wevers et al. 2019](#)) as well as rapidly-launched jets (e.g., [Bloom et al. 2011](#); [Burrows et al. 2011](#); [Mattila et al. 2018](#)).

Despite occasionally swallowing stars, SMBHs are believed to grow mainly by accreting surrounding gas during their active galactic nuclei (AGN) phases. Stochastic variability is ubiquitous in AGNs, among which a small fraction are extremely variable with light curve featured as flaring (e.g., [Graham et al. 2017](#)) or state changing (e.g., [Graham et al. 2020](#)) pattern. Follow-up spectroscopic observations of the most variable AGNs suggest they can even change their types on time scales of years, characterized by appearance or disappearance of broad emission lines (e.g., [Shappee et al. 2014](#); [LaMassa et al. 2015](#); [Runnoe et al. 2016](#); [MacLeod et al. 2016](#); [Yang et al. 2018](#)). These objects are dubbed as changing-look (CL) AGNs, and their variation is driven by the dramatic change of the accretion flow rather than the obscuration ([Sheng et al. 2017](#); [Hutsemékers et al. 2019](#)). The most intriguing subclass could be the so-called "turn-on" AGNs, which transition from a quiescent galaxy to a type 1 AGN within several months to years. Although only few such systems have been confirmed ([Gezari et al. 2017](#); [Yan et al. 2019](#); see also [Frederick et al. 2019](#)), they appear to not be extremely rare, and even one poses challenges to canonical accretion disk theories.

In a nutshell, the known extragalactic transient sky is dominated by SNe and transient SMBH accretion. The investigation of latter has been facilitated recently by improved time-domain surveys. Current large surveys have been exclusively performed in the optical band, which are blind to transients that are either self-obscured (e.g. type 2 AGNs) or located in the dusty regions (e.g. SNe). Therefore, it is crucial to conduct surveys in bands free of dust obscuration. In this sense, the mid-infrared (MIR) is the most promising band but it was completely unexplored until the *spitzer* Deep Wide-Field Survey, which has now been incorporated into the Decadal IRAC Boötes Survey. This survey is used to search for obscured SNe and to study the quasar variability in the MIR ([Kozłowski et al. 2010, 2016](#)) by taking advantage of the repeatedly surveyed region ( $\sim 9 \text{ deg}^2$ ). SPitzer InfraRed Intensive Transients Survey (SPIRITS, [Kasliwal et al. 2017](#)) is a more recent project dedicated to finding infrared luminous transients by targeting 190 nearby galaxies, which has yielded out numerous hidden SNe and dusty stellar outburst ([Jencson et al. 2019](#)). Despite this, such projects generally focused on a small sample of galaxies or a small sky region, so they are almost incapable of capturing rare events like TDEs as well as "turn-on" AGNs.

Fortunately, the *Wide-field Infrared Survey Explorer* (*WISE*) mission ([Wright et al. 2010](#)) and its asteroid-characterization extension, the Near-Earth Object Wide-field Infrared Survey Explorer Reactivation (*NEOWISE*) mission ([Mainzer et al. 2014](#)), have opened a new window to map the MIR dynamic sky benefited from its ideal survey mode (see §2.1). For instance, [Sheng et al. \(2020\)](#) have come up with an efficient method to look for CL AGNs from MIR-variable quasars screened by *WISE* light curves (see also [Stern et al. 2018](#); [Assef et al. 2018](#)) but with the caveat that only "turn-off" CL AGNs can be selected because of their parent sample of quasars. [Wang et al. \(2018\)](#) used *WISE* to systematically search for TDEs in extremely variable normal galaxies and discovered IR echoes of TDEs, immediately after the pioneering discoveries of IR echoes of TDEs ([Jiang et al. 2016](#); [Dou et al. 2016](#); [van Velzen et al. 2016](#)). However, [Wang et al. \(2018\)](#) select variables using the variability flag given by *WISE* pipeline, which is on basis of data taken between 2009 December and 2011 February. As a result, the acquired galaxies have all entered the stage of dimming, which make the further confirmation of their physical nature unrealistic.

To overcome the limitation from [Wang et al. \(2018\)](#), we have designed a new project to search for and explore MIR Outburst in Nearby Galaxies (MIRONG) specifically. MIRONG uses both the public *WISE* and *NEOWISE* databases to search for more recent outburst events in galaxies and enable multi-wavelength follow-up. MIRONG may uncover a population of extragalactic transients which have been overlooked by traditional optical surveys and ultimately

improve our understanding of the extragalactic dynamic sky. The paper is organized as follows. In Section 2, we describe the process of sample selection of MIRONG. In Section 3-5, we characterize the sample from properties of MIR light curves, event rate and luminosity function, and their host galaxies, respectively. We inspect the nature of MIRONG in Section 6 and discuss the implications of our work in Section 7. Finally, we end with a brief summary and discussion of future prospects in Section 8. We assume a cosmology with  $H_0 = 70 \text{ km s}^{-1} \text{ Mpc}^{-1}$ ,  $\Omega_m = 0.3$ , and  $\Omega_\Lambda = 0.7$ .

## 2. SAMPLE SELECTION

### 2.1. Characteristics of WISE and NEOWISE Survey

WISE has performed a full-sky imaging survey in four broad bandpasses centered at 3.4, 4.6, 12 and 22  $\mu\text{m}$  (labeled W1-W4) from 2010 January to August. WISE continued surveying the sky in its bluest three bands during 2010 August and September. After that, its NEOWISE hunted asteroids until 2011 February (Mainzer et al. 2011), with only the W1 and W2 channels remaining operational as the solid hydrogen cryogen used to cool the W3 and W4 instrumentation has been depleted. Following a 33 month hibernation period, the WISE instrument recommenced survey operations in 2013 December (Mainzer et al. 2014). This post-hibernation mission is referred to as NEOWISE-Reactivation (NEOWISE-R) to hunt for asteroids that could pose an impact hazard to the Earth.

The WISE survey strategy is very novel. It has a field-of-view of  $47' \times 47'$  and a small (10%) overlap between adjacent fields in one orbit. The scan circle advances by about  $4'$  per orbit and 15 orbits can be fulfilled each day. Therefore, for a typical sky region, the available exposures can be segmented into a series of 1 day time intervals (referred to as visits), with such visits occurring once every six months except for the gap during the hibernation. As a spontaneous outcome of the unique survey mode, it becomes an unprecedented database to study the transient MIR sky. There are typically 12 successive orbits covering a given source within one day, with denser coverage toward higher ecliptic latitude (Wright et al. 2010; Hoffman et al. 2012). Such a high-frequency sampling allows us to probe the intraday MIR variability, which was seldom explored in the past (e.g., Jiang et al. 2012; Jiang 2018).

The NEOWISE survey is still ongoing at the time of submission of this paper. Our sample selection is based on the WISE and NEOWISE-R data from 2010 to the end of 2018, that is all of the available data when we did this work. They have yielded an average of 12 visits for each target, so an investigation of MIR variability on year time scales is absolutely achievable for a large sample as proved by previous works (e.g., Wang et al. 2018). We have noticed that the latest NEOWISE data release (2020 March 26) has come out

just before our paper submission, while it is a massive work to redo our work from the very beginning by including the newly released data from 2018 December to 2019 December. However, the newest photometry has been added in the analysis of our final sample of MIRONG since the more complete light curves will help us obtain more accurate quantities (e.g., peak luminosity).

### 2.2. Parent Sample

The Sloan Digital Sky Survey (SDSS) has spectroscopically observed millions of galaxies with apparent Petrosian magnitude  $r < 17.77$  (Strauss et al. 2002). We have checked the SDSS DR14 spectroscopic catalog (Abolfathi et al. 2018) and picked out those flagged with "GALAXY" class at  $z < 0.35$ , that is 1,253,962 spectra in total. Note that some of them are repeated multi-epoch data for same objects, there are 1,150,901 unique objects differentiated by their celestial coordinates. We choose spectroscopic galaxies instead of photometric because we need to know our galaxies' redshift ( $z < 0.35$ ) and other properties. The redshift cut is to ensure that the  $H\alpha$  region is located in the wavelength range of SDSS spectrum, which will help us diagnose the spectral type by emission-line ratios in the Baldwin-Phillips-Terlevich diagnostic diagram (BPT diagram in short, Baldwin et al. 1981). Second, the cut of  $z < 0.35$  will keep the dust emission within the WISE bands as it is expected to start at 2  $\mu\text{m}$ . Furthermore, the signal-to-noise ratio (S/N) of more distant galaxies are generally too low to undertake variability studies accurately. We designate these  $\sim 1$  million galaxies the parent sample.

### 2.3. MIR-variable Galaxies

We construct a sample of MIR-variable galaxies in advance of the final selection of outbursts. We retrieved the W1 and W2 profile-fit photometry of each galaxy in the parent sample from the public AllWISE Multiepoch Photometry Table and NEOWISE-R Single Exposure (L1b) Source Table<sup>2</sup>, encompassing all exposures from 2010 up to 2018. The photometry is measured by point spread function (PSF) profile fitting, in which the PSFs have been estimated from observations of many tens of thousands of stars. The AllWISE Multiframe pipeline detects sources on the deep coadded atlas images, and then measures the sources for all available single-exposure images in all bands simultaneously while the NEOWISE magnitudes are obtained by PSF-fit to individual exposures directly.

The acquired single-exposure data are first filtered by the quality flags marked in the catalogs. The bad data points with poor quality frame ( $qi\_fact < 1$ ), charged particle hits

<sup>2</sup> <https://irsa.ipac.caltech.edu/cgi-bin/Gator/nph-scan?mission=irsa&submit=Select&projshort=WISE>

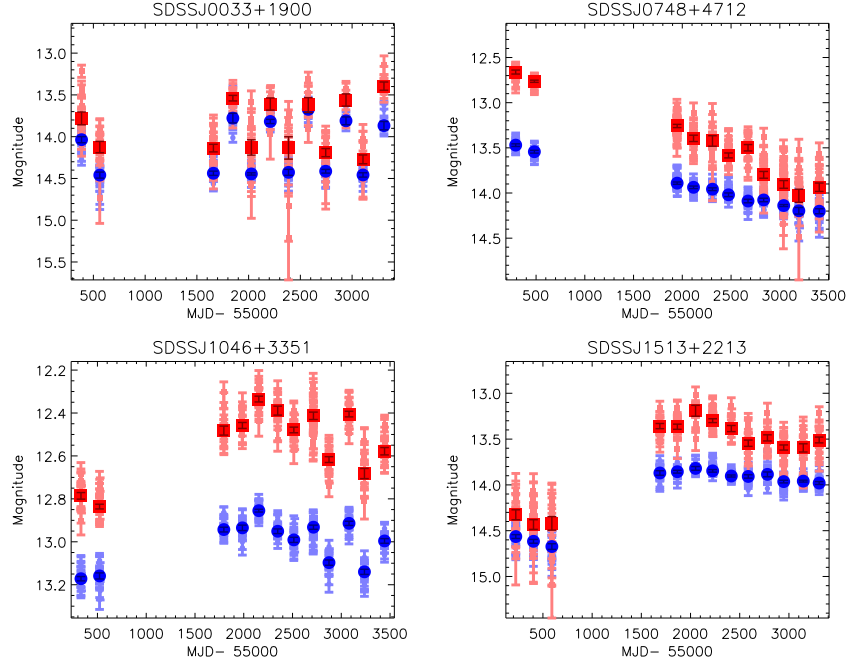


**Figure 1.** We show the different *WISE* light curves patterns of the MIR-variable galaxies, including the periodic oscillation (top left), long-term declination (top right), stochastic variations (bottom left) and state transition (bottom right). The recent flare-like patterns are presented separately in Figure 2. Blue dots: W1 ( $3.4\mu\text{m}$ ); red squares: W2 ( $4.6\mu\text{m}$ ). The raw single exposures are plotted in light blue and red, while the binned data are plotted in dark blue and red. As we explained in §2.3, the case of one-year cycle oscillation (top left) is not physical but caused by the latent image artifact from a nearby bright star.

( $saa\_sep < 5$ ), scattered moon light ( $moon\_masked = 1$ ) and artifacts ( $cc\_flags \neq 0$ ) have been removed. In addition, we have also abandoned the photometry fitted with multiple PSF components ( $nb > 1$  and  $na > 0$ ), that is performed when the source is fit concurrently with other nearby detections or when a single object is split into two components during the fitting process. The surviving data are immediately binned every half year to increase the S/N of the photometry, resulting in average 13 epochs for each target. This binning strategy fits to the sampling rate of *WISE* survey (see §2.1). We begin to perform a blind search of variable galaxies which satisfy  $\delta W1 > 0.5$  or  $\delta W2 > 0.5$ .  $\delta W1$  ( $\delta W2$ ) are the difference between the maximum and minimum values of W1 and W2 across the combined *ALLWISE*+*NEOWISE* light curves. We have further requested  $\delta W1 > 0.3$  or  $\delta W2 > 0.3$  during the *NEOWISE* phase to make sure the variability is still obvious after 2013 December for ease of follow-up studies. The latter condition has also excluded fake variable sources caused by possible systematical offset between *ALLWISE* and *NEOWISE* photometry. The significance of the variability are required to be not lower than  $5\sigma$ , that is  $(W^{?max} - W^{?min}) / \sqrt{(W^{?max\_err})^2 + (W^{?min\_err})^2} > 5$ , to ensure that the variability is still valid when taking uncertainties into consideration. Last, we have casted away faint sources by the cut  $W2min < 14$  to obtain a magnitude limit sample.

The above cut of variability amplitude has resulted in a sample consisting of 1,026 galaxies<sup>3</sup>, allowing for us to check visually their MIR light curves one by one. While stochastic variability is predominant, peculiar variability patterns are also visible (see Figure 1), such as state transition, long-term declining and flare-like rising light curves. We notice that very few of them (11 objects) show periodic oscillations with a cycle of one year (see the example in the top left panel of Figure 1). These objects are affected by the latent image artifact from a nearby bright star that appears in the preceding image in the scan<sup>4</sup>. The photometry pipeline has often failed to flag them automatically so that the one-year cycle variations may not be real. In addition, we emphasize that our selection of the MIR variable sources is conservative, and the actual fraction of these galaxies may be much higher than 0.1% as we inferred here.

<sup>3</sup> The general information of the 1,026 variable galaxies can be downloaded from this website: [http://staff.ustc.edu.cn/~jnac/data\\_public/wisevar.txt](http://staff.ustc.edu.cn/~jnac/data_public/wisevar.txt)

<sup>4</sup> The *WISE* scan direction on the sky flips every 6 months as the orbit precesses around the sky. Hence a particular point on the sky will alternate being scanned north-to-south and south-to-north each 6 months. This means that the bright star that is seen on the preceding image in one epoch will be seen on the following image 6 months later. As a consequence, the artifact affects with one year cycle. The polluted photometry should have been flagged as "P" in "cc\_flags" but the flag does not work well when the source is slightly offset from the predicted position of the latent and the expected size of the latent is poorly modeled.



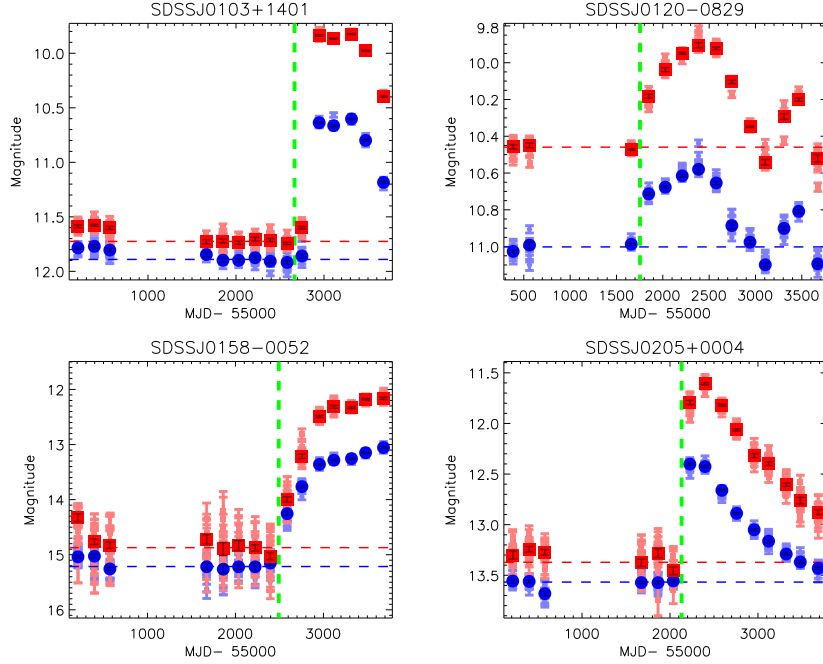


**Figure 2.** Similar to Figure 1, the *WISE* light curves of four representative outburst galaxies in our MIRONG sample. The estimated magnitudes at the quiescent phase are shown with dashed blue and red lines. The vertical green dashed lines mark the boundary of the quiescent and outburst stage. SDSSJ0103+1401 shows very fast rising followed by a relatively stable high state, in contrast with SDSSJ0205+0004, which displays also fast rising but immediate declining. The other two objects shows a slower rising, in which SDSSJ0120-0829 has manifested itself as a complete flare in terms of both rising and declining (Sun et al. 2020).

#### 2.4. Sample of MIRONG: Galaxies with MIR Outburst

For the purpose of this study, we further selected a sub-sample of MIR outburst galaxies, which initially display a stable phase yet followed by a significant brightening seen in the MIR light curves. The emission in the quiescent state is served as the background that will be subtracted from the outburst light curves. We estimated the pre-outburst magnitudes by adopting the median value of the data points in the quiescent state. The beginning of outburst is set to the epoch when either W1 or W2 magnitude shows a brightening over  $3\sigma$  significance. We adopted two criteria to qualify a flare: (1) the maximum flux density after outburst has brightened by  $> 0.5$  mag in W1 or W2 with respect to the quiescent state ( $\Delta W1 > 0.5$  or  $\Delta W2 > 0.5$ ); (2) the variability significance at the epoch of maximum flux is larger than  $5\sigma$  in at least one band. The above criteria are effective, with which we yield 148 MIR outburst sources. Lastly, we caution that the *WISE* spatial resolutions at W1 and W2 bands are of  $\sim 6''$ , so the photometry could suffer from the contamination of nearby sources. Thus, we rejected those targets with companions (galaxy pairs or polluted by foreground stars) within project distance closer than  $6''$  by checking their SDSS images visually. As a result, 137 objects are left, constituting the final outburst sample (see basic parameters in Table 1 and four representative examples in Figure 2). The median redshift is 0.102 (see Figure 3).

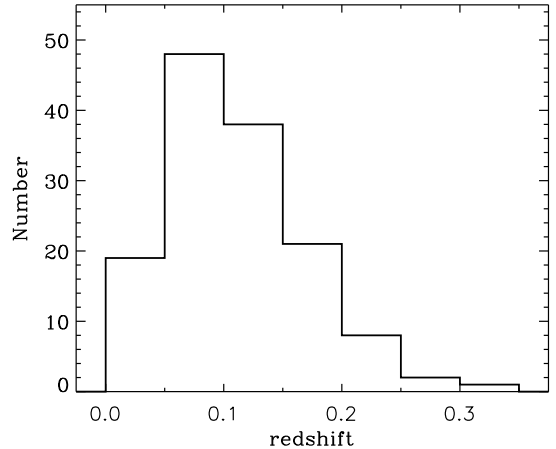


**Figure 3.** The histogram of redshift of our sample.

To summarize, we have finally selected a well-defined sample of 137 MIR outburst nearby galaxies (MIRONG) which display a brightening over 0.5 mag with respect to the previous quiescent phase in the *WISE* light curves. These galaxies are all initially drawn from the SDSS spectroscopic catalog with rich available information, e.g., properties of host galaxies and nuclear activity (see §5), which allows for further detailed study on the nature of transient MIR emission in the center of galaxies.

### 3. PROPERTIES OF MIRONG

#### 3.1. Optical Counterparts

It is natural to ask whether these MIR flares have been detected by various optical surveys. First, we cross-matched our sample with (candidate) SNe catalog (Gal-Yam et al. 2013)<sup>5</sup> discovered between 2010 and 2018 and yielded 11 objects. In addition, we have also added four more objects that are reported in literature but not listed in the SNe catalog, including two Gaia nuclear transients (SDSSJ0854+1113, SDSSJ1647+3843; Kostrzewa-Rutkowska et al. 2013), one CRTS outburst event (SDSSJ1332+2036, Drake et al. 2019) and another turn-on quasar discovered by iPTF (SDSSJ1554+3629, Gezari et al. 2017). The basic information about the known 15 optical transients is presented in Table 3.

Among these sources, SDSSJ0936+0615, SDSSJ1531+3724, SDSSJ1540+0054 and SDSSJ1554+1636 are spectroscopically confirmed SNe discovered by ASAS-SN. SDSSJ0158-0052 is a candidate TDE discovered by Pan-STARRS and ASAS-SN, which occurred in a Seyfert 1 galaxy with low mass black hole (Blanchard et al. 2017), whose MIR flare has been successfully explained by the dust echo of the AGN torus (Jiang et al. 2017). SDSSJ1554+3629, SDSSJ0915+4814 and SDSSJ1133+6701 are newly reported turn-on AGNs which have transferred from LINERs to quasars within a few of years (Gezari et al. 2017; Frederick et al. 2019). SDSSJ1620+2407 is a candidate TDE discovered by ATLAS, which shows markedly newly-appeared broad Balmer lines and blue continuum (Fraser et al. 2017). Apart from the nine studied objects above, the remaining six sources have only been alerted by photometry without further spectroscopic observations. Despite lack of reliable identifications, in contrast with the four SNe cases ( $>1''$ ), their close distance to the galactic center ( $<1''$ ) suggests that they are likely associated with the SMBH activity rather than stellar explosion.

For the remaining 120 galaxies for which no known optical counterparts are matched, we have also examined the public CRTS (Drake et al. 2009) and ASAS-SN (Kochanek et al. 2017) data. The combined data give V-band light curves spanning from 2005 to 2018. We did not find any optical flares, implying the faintness of optical emission for most, if not all, MIR bursts galaxies.

#### 3.2. Constrains on the Physical Position of MIR flares

The specific locations in the galactic region of the MIR flares can give us strong clues to their nature. For example, an outburst offset from the galactic center can be convincingly

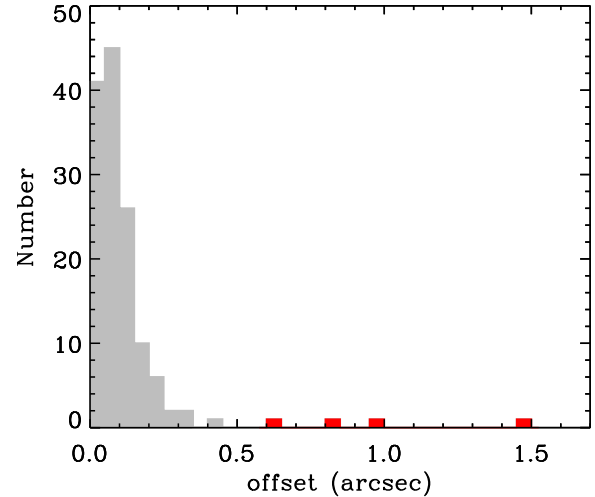


**Figure 4.** The histogram of center offset distance ( $\Delta d$ ) in unit of arcsec, defined as the angular distance of the photometric center at the maximum epoch and the quiescent epoch. The  $\Delta d$  of SNe (highlighted in red) are all larger than  $0''.5$  in contrast with the tiny values of other objects (median  $0''.08$ ).

classified as SNe. Otherwise the central SMBHs might be considered as the most likely origin.

The astrometry of *WISE* catalog has been reconstructed with respect to the 2MASS Point Source Catalog reference frame. The root mean square error of the position is found to be less than  $0.5''$ , for sources with  $\text{SNR} > 20$  in at least one *WISE* band, where the noise includes flux errors due to zodiacal foreground emission, instrumental effects, source photon statistics, and neighboring sources<sup>6</sup>. The *WISE* PSF profile-fit photometry we used is measured at the intensity-weighted center, so the variation of the center position can tell us whether or not the outburst is far away from the pre-outburst galactic center. For instance, when an off-centered SNe has exploded and is MIR bright, there should be a positional offset between the *WISE* photometric center of its host galaxy and the intensity-weighted center determined by the SNe outburst.

To test whether there significant positional offsets exist, we have calculated the mean photometric center (RA, DEC) given by ALLWISE and NEOWISE-R catalog at the quiescent state and that from the maximum outburst epoch, respectively. We defined the angular distance between them as the offset distance ( $\Delta d$ , in unit of arcsec). The distribution of  $\Delta d$  is presented in Figure 4. The majority of our galaxies show very small  $\Delta d$  with a median value of  $0''.08$ . We noticed that only the four known SNe (see §3.1) have  $\Delta d$  larger than  $0''.5$  (1.48, 0.99, 0.63 and 0.83 arcsec), which is ex-

<sup>5</sup> <http://rochesterastronomy.org/supernova.html>, noting that they are not all real SNe, but candidates including nuclear transients.

<sup>6</sup> [http://wise2.ipac.caltech.edu/docs/release/allsky/expsup/sec6\\_4.html](http://wise2.ipac.caltech.edu/docs/release/allsky/expsup/sec6_4.html)

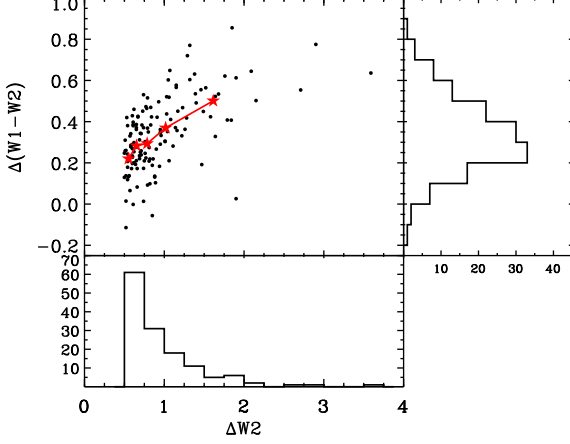


**Figure 5.** The color variation  $\Delta(W1 - W2)$  versus  $W2$  variability amplitude ( $\Delta W2$ ) of the MIR outburst galaxies. The histogram of  $\Delta(W1 - W2)$  and  $\Delta W2$  are shown in the right and bottom panels, respectively. We have divided the whole sample into five equal-sized subsample sorted by  $\Delta W2$  and plotted the median  $\Delta(W1 - W2)$  of each subsample as red five-point stars. The MIR variability shows a overall trend of redder when brighter.

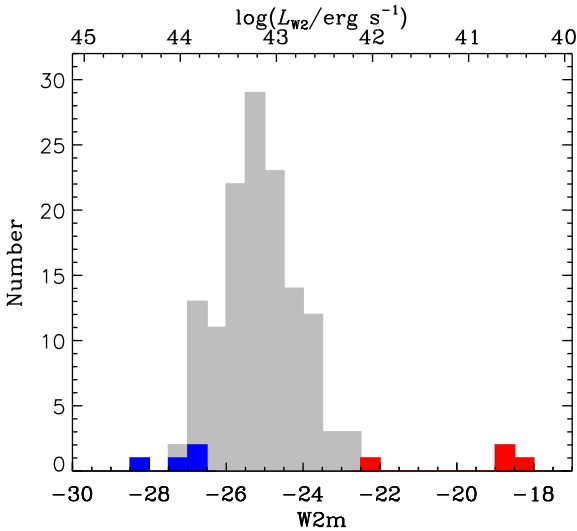


**Figure 6.** The histogram of peak absolute  $W2$  magnitude. We plot the confirmed SNe in red and radio-loud AGNs in blue.

pected since their optical offsets are known as large as 2.93, 1.93, 1.20 and 1.00 arcsec, respectively. It demonstrates that checking for the shift of photometric center appears effective in recognizing a candidate outburst located larger than  $1''$  from the nucleus.

### 3.3. The MIR Light Curves

Since bulk of our MIR flares have no informed optical counterparts, we instead try to characterize their properties by the MIR light curves themselves. The whole sample has brightened by average 0.63 (median 0.53) and 0.96 (0.79)

magnitudes in  $W1$  and  $W2$ , respectively, indicating that the variability amplitude at  $W2$  band is overall larger than  $W1$ . In other words, the  $W1$ - $W2$  color displays a trend of redder-when-brighter (RWB, see Figure 5) with a median  $\Delta(W1 - W2) = 0.33$ . Only two Seyfert galaxies (SDSSJ0811+4054, SDSSJ1029+2526) show the color changes in an opposite way. The RWB evolution is consistent with the scenario found in CL AGNs, indicating a higher hot dust contribution than the starlight-dominated quiescent state when the AGN activity becomes stronger (e.g., Sheng et al. 2017; Yang et al. 2018).

In order to investigate further the properties of the MIR outbursts, we subtracted the background emission from the light curves in the flare state (Section 2.4). The background-subtracted  $W2$  absolute magnitude ( $W2_m$ ) is presented in Figure 6, with the majority (95.6%, 131 out of 137) ranging from  $-22.5$  to  $-27$ , corresponding to the logarithmic monochromatic luminosity ( $\log L_{W2}$ ) between 42 to 44. It is conspicuous that while the low-luminosity outliers ( $W2_m \gtrsim -22.5$  or  $\log L_{W2} \lesssim 42$ ) are all SNe, the radio-loud AGNs (see §6.2) dominate at the high-luminosity end. We stress that the minimum absolute magnitudes (or maximum luminosity) do not always tell us the true peak since some of them are still rising in the light curves. If we naively suppose that the MIR outburst started from the middle between the first brightening data point and the quiescent state, median rising timescale to the (current) peak is 429 days, or 398 days in the rest-frame of galaxies.

### 3.4. Dust Properties

In this subsection, we try to acquire more physical quantities by fitting the MIR emission with dust thermal emission scenario. For dust grains with size distribution  $N(a)$  ( $a$  is the radius of grain sphere), density  $\rho$  and absorption coefficient  $Q_\nu$  at luminosity distance  $d_L$ , the observed monochromatic flux at a given frequency can be calculated as below (see also Wang et al. 2019).

$$f_\nu = \frac{1}{4\pi d_L^2} \int_{a_{\min}}^{a_{\max}} N(a) 4\pi a^2 Q_\nu(a) \pi B_\nu(T) da$$

$$= \frac{3M_d}{4\rho d_L^2} \left\langle \frac{Q_\nu}{a} \right\rangle B_\nu(T) \quad (1)$$

where

$$\left\langle \frac{Q_\nu}{a} \right\rangle = \frac{\int_{a_{\min}}^{a_{\max}} N(a) a^3 (Q/a) da}{\int_{a_{\min}}^{a_{\max}} N(a) a^3 da}; \quad (2)$$

$$M_d = \int_{a_{\min}}^{a_{\max}} N(a) \rho \frac{4}{3} \pi a^3 da \quad (3)$$

For simplicity, we assume that the dust grains follow a MRN size distribution (Mathis et al. 1977; see also Draine &

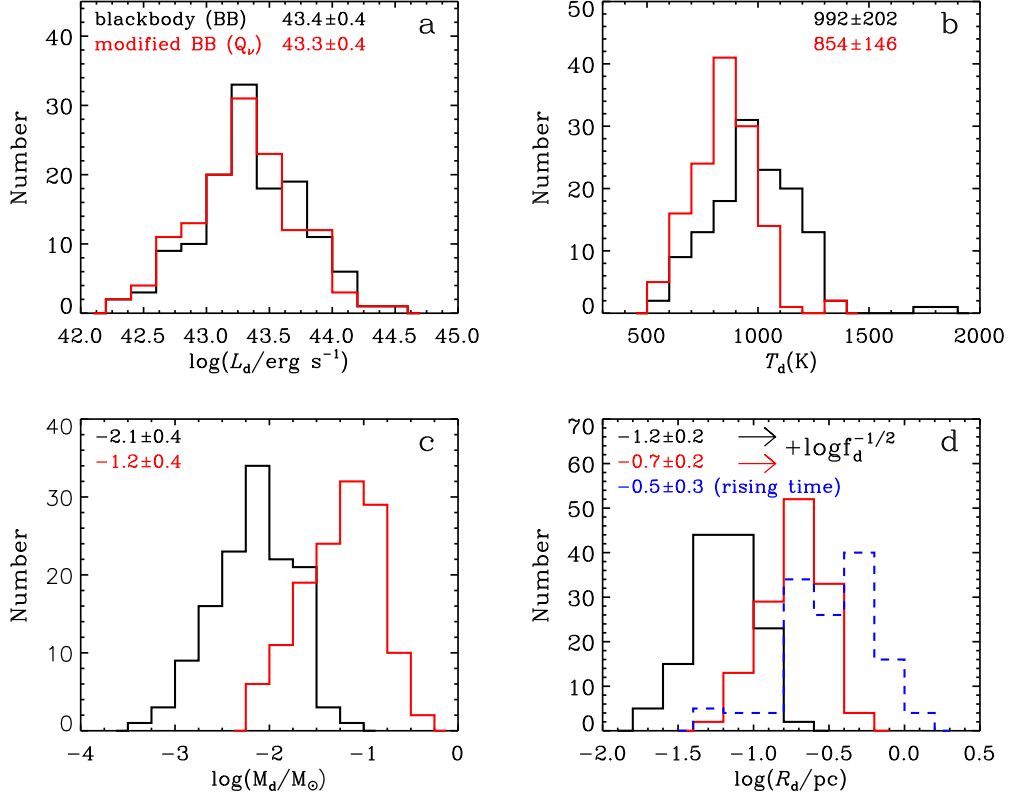


**Figure 7.** The histograms of the fitted dust luminosity (panel *a*), temperature (*b*), mass (*c*) and distance to the heating source (*d*), respectively. All parameters are derived at the W2 maximum epoch. The black line represents the pure blackbody case while the red shows the fitting with dust absorption efficiency taken into consideration. The numbers indicated in the panels are medians and standard deviations of the distributions. The four SNe sources have not been shown in the plots as they are outliers in the low end whose values can be retrieved in Table 2. For the dust distance (panel *d*), we have also overplotted the distance given by the rising time scale of the *WISE* light curves (blue dashed line). The right pointing arrows indicate that the black and red histograms will shift by  $\log f_d^{-1/2}$  if the real dust covering factor ( $f_d$ ) is not unity.

Lee 1984) as  $N(a) \propto a^{-3.5}$  with  $a_{\min} = 0.01 \mu\text{m}$ ,  $a_{\max} = 10 \mu\text{m}$  and an average density of  $\rho = 2.7 \text{g cm}^{-3}$  for silicate grains.

We begin the fit with blackbody model ( $Q_\nu = 1$ ). However, the real dust emission is not perfect blackbody and the absorption coefficient should be considered. We adopt the silicate absorption coefficients in Laor & Draine (1993), which gives  $\langle \frac{Q_\nu}{a} \rangle = 0.214$  and  $0.177$  in W1 and W2, respectively. The fluxes in W1 and W2 are then fitted with the modified blackbody model to derive the dust temperature ( $T_d$ ) and mass ( $M_d$ ). The luminosity is comparable to that obtained with a simple blackbody model, while the  $T_d$  is systematically lower and  $M_d$  is about one order of magnitude higher (see Figure 7). We note that the  $T_d$  are all below 1500 K, in agreement with the suppression of the sublimation temperature of silicate and graphite grains (Barvainis 1987; Mor & Netzer 2012). All the blackbody parameters to describe the dust emission at the epoch of luminosity maximum can be found in Table 2 and their distributions are presented in Figure 7.

We then attempted to estimate the distance of dust emission ( $R_d$ ) to the central radiation source. By assuming spher-

ical symmetry for the dust distribution the distance of dust emission can be expressed by

$$R_d = \left( \frac{L_d}{4\pi\sigma T_d^4} \right)^{1/2}, \quad (4)$$

As the dust distribution is uncertain, the above estimation may be oversimplified but can be treated as a strict lower limit on the scale of dust distribution (median value of 0.06 pc). In reality, the dust might not fully cover the central radiation source. If the dust covering factor is  $f_d$  (with unity as complete coverage), the corresponding distance should be increased by a factor of  $f_d^{-1/2}$ . Likewise, the  $R_d$  for the case of modified blackbody model would be also larger, yielding a median value of 0.20 pc ( $f_d = 1$ ) that is scaled by the dust mass. Alternatively, the MIR rising time scale can be also used as a distance indicator of the dust responsible for the peak emission. In this way, we obtain a median value of 0.34 pc given the median rest-frame rising time scale of 398 days.  $f_d = 0.04$  (or  $f_d = 0.34$ ) from the blackbody (or modified blackbody) fit can generally reproduce the observed rising time scale. Above all, we may conclude that the dust is



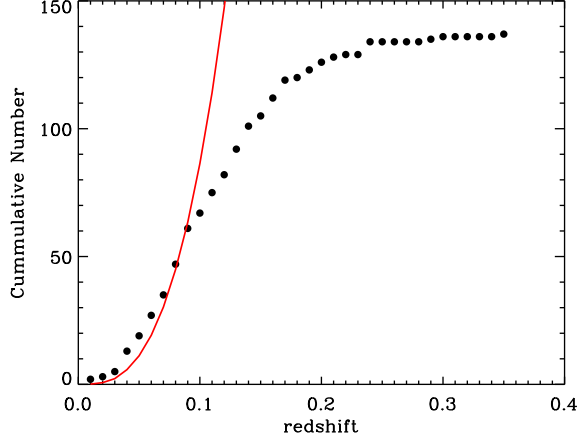


**Figure 8.** The accumulated redshift distribution of our sample. The curve shows the comoving volume of SDSS footprint at the corresponding redshift multiplied by  $1.2 \times 10^{-6} \text{ Mpc}^{-3}$ .

located at the order of  $0.1 \text{ pc}$  (see distribution in panel *d* of Figure 7) with covering factor at the order of 0.1.

#### 4. EVENT RATE AND LUMINOSITY FUNCTION

##### 4.1. Event Rate Estimation

Regardless of their physical nature, we try to estimate the event rate of the MIRONG selected by us with the same manner used in Wang et al. (2018). The accumulative number is roughly proportional to the comoving volume up to  $z \sim 0.09$ , then the increase rate becomes slower and finally flattens (see Figure 8). It suggests that the sample can be taken as almost complete at  $z < 0.09$  but obviously under-representative at  $z > 0.09$  if there is no evident redshift evolution in the event rate. There are 61 objects at  $z < 0.09$ , yielding a density of  $1.2 \times 10^{-6} \text{ Mpc}^{-3}$  in the SDSS sky region.

On the other hand, we note that the SDSS main galaxy surveys are originally designed to target galaxies with dereddened  $r$ -band magnitudes brighter than 17.77 (Strauss et al. 2002). The cut ensures that galaxies with  $r$ -band absolute magnitudes of  $M_r < -19.5$  are complete, which corresponds to the luminosity range for most galaxies in our sample (Figure 11). Considering only for galaxies with  $M_r < -19.5$  at  $z < 0.09$  will result in a density of  $2.2 \times 10^{-4} \text{ gal}^{-1}$ . Since our sample selection requires a brightening phase in the *NEOWISE* stage (spanning 5 years) and average rising timescale of about one year, the event rate should be divided by a factor of four to obtain the rate per year. The final event rate is about  $5.4 \times 10^{-5} \text{ gal}^{-1} \text{ yr}^{-1}$  and the corresponding density rate is  $3.0 \times 10^{-7} \text{ Mpc}^{-3} \text{ yr}^{-1}$ , that is basically consistent with  $10^{-7} \text{ Mpc}^{-3} \text{ yr}^{-1}$  given by Wang et al. (2018).

##### 4.2. Peak Luminosity Function

We use the  $V/V_{max}$  method (Schmidt 1968; Eales 1993) to calculate the MIR peak luminosity function of the outburst.

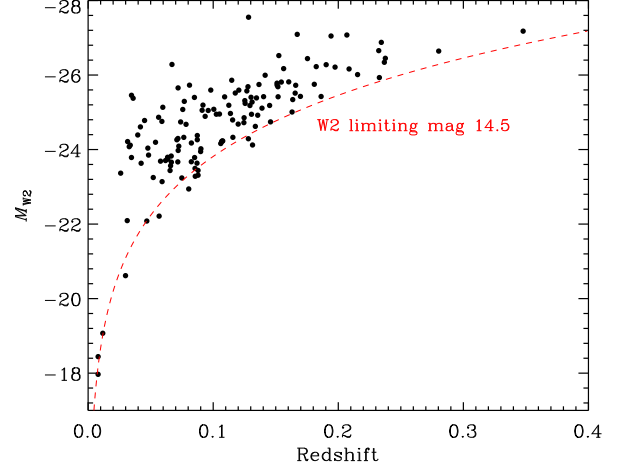


**Figure 9.** The host galaxy W2 absolute magnitudes (quiescent state) of our sample, which decreases with the redshift. The red dashed line denotes the limiting magnitude 14.5.

The formula is adopted as below

$$\Phi(L)dL = \sum_{L_i \in [L-\Delta L/2, L+\Delta L/2]} \frac{1}{V_{max} f_{comp}}. \quad (5)$$

Here  $V_{max}$  is the maximum comoving volume within which the galaxy of interest is detectable at a given depth. Taking 17.77 and 14.5 as the limiting magnitude at  $r$ -band and W2, respectively, we computed the  $V_{max}$  for each target. In its simplest form,  $\Phi(L)$  is the sum of  $1/V_{max}$  for all objects in each luminosity bin. The limiting magnitude of 14.5 at W2 band is determined from our cut  $W2_{min} < 14$  and a brightening amplitude of  $> 0.5 \text{ mag}$  (see §2.3), which is verified by the magnitude-redshift distribution of the final MIRONG sample (see Figure 9).  $f_{comp}$  is the completeness for sources locating in the SDSS footprint that have been spectroscopically observed. The spectroscopic effective area of the SDSS DR14 catalog is  $9,376 \text{ deg}^2$  (the full sky is  $41252.96 \text{ deg}^2$ ) and about 92.8% of the galaxies at  $r < 17.77$  have been included in the main galaxy sample (Lazo et al. 2018), thus  $f_{comp} = \frac{0.928 \times 9376}{41252.96} = 0.211$ .

The luminosity function in log-log space with  $\log L_{W2}$  bin 0.5 is shown in Figure 10. We estimate the statistical errors using the bootstrap method. To this end, we generate  $N = 1000$  bootstrap samples, each of which consists of objects picked randomly from the original sample. The errors are then given by the standard deviation in the distribution of  $\Phi$  measured from the bootstrap samples. The Schechter function is typically used to characterize galaxy luminosity functions (Schechter 1976) in the form of

$$\Phi(L)dL = \left(\frac{\Phi^*}{L^*}\right) \left(\frac{L}{L^*}\right)^\alpha e^{-L/L^*} dL, \quad (6)$$

where  $L$  is galaxy luminosity,  $L^*$  is the characteristic luminosity where the power-law form of the function cuts off and

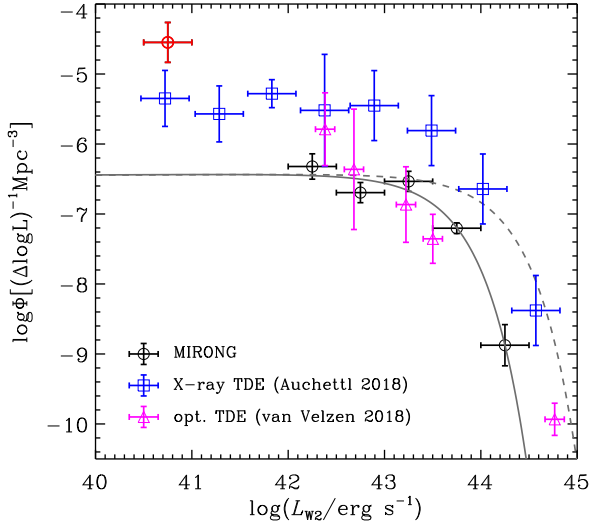


**Figure 10.** The W2 peak luminosity function of our MIRONG sample. The data points are plotted with  $\log L_{W2}$  ranging from 40.5 to 44.5 (bin 0.5). The faint end ( $\log L_{W2} \in [40.5, 41]$ ) is totally contributed by extremely low-redshift SNe (red circle). The high end ( $\log L_{W2} > 42$ ) is fitted by a single Schechter function (grey line). The shifted grey dashed line depicts the luminosity function of the primary emission which causes the MIR outburst assuming a dust covering factor of 0.3. We have also overlaid the observed X-ray (blue squares, data from Fig. 6 of Auchettl et al. 2018) and optical (magenta triangles, data from Fig. 1 of van Velzen 2018) luminosity functions of TDEs for comparison.

the parameter  $\Phi^*$  is the normalization. We try to fit the luminosity function at the high end with a single Schechter function, yielding  $\log \Phi^* = -2.92$ ,  $\log L^* = 43.50$  and  $\alpha = -0.05$ . The sources at the very faint end of  $\log L_{W2}$  ( $< 41$ ) are occupied by SNe and appear as a distinct population from the high end, thus we have ignored them in the fitting. The luminosity function drops quickly at the very high end. The flattening at  $\log L_{W2} \lesssim 43$  could be due to the selection effect that requires a brightening amplitude greater than 0.5 mag. It is possible that there are more fainter outbursts with relatively low brightening amplitudes ( $< 0.5$  mag), but missed by our selection.

## 5. HOST GALAXY AND CENTRAL BLACK HOLE

### 5.1. Host galaxy properties

The host galaxy property is crucial to understand the nature of MIRONG. It is well known that galaxies show a bimodal distribution in the colour-magnitude diagram (CMD), which are mainly clustered into a red sequence and blue cloud (e.g., Strateva et al. 2001; Bell et al. 2004) with a green valley in between. We retrieved the apparent *ugriz* Petrosian magnitudes from the SDSS DR14 and then corrected for the extinction using the dust maps of Schlegel et al. (1998). For a fair comparison of galaxies at different redshifts in the CMD, we applied *k*-corrections to the observed magnitudes to  $z = 0.1$

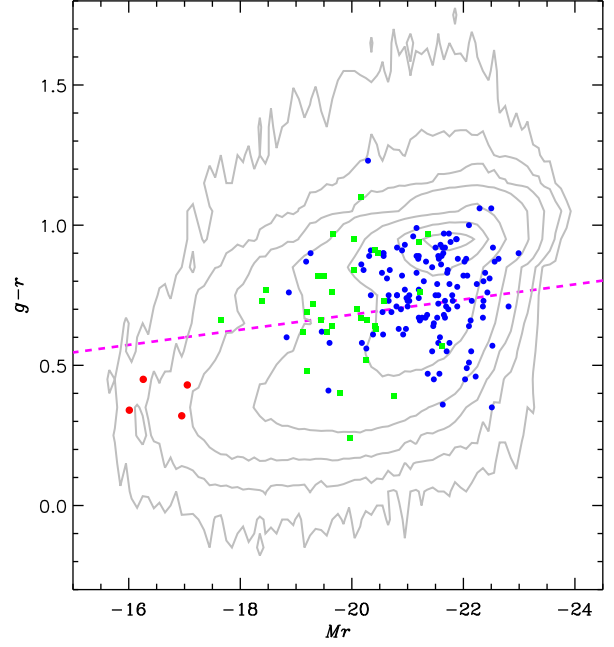


**Figure 11.** The color-magnitude diagram ( $g-r$  vs.  $M_r$ ) of the MIRONG sample (blue filled circles). The magnitudes and color are displayed after correction for Galactic dust extinction and *k*-correction to  $z = 0.1$ . We denote the four SNe host galaxies in red. Contours show the density of low-redshift ( $z < 0.2$ ) SDSS DR7 spectroscopic galaxies. The contour lines correspond to 5, 25, 100, 400, 2000, 5000 and 8000 galaxies per bin of  $\Delta(g-r) = 0.1$  and  $\Delta M_r = 0.1$ . The magenta dashed lines is the assigned line of demarcation between the blue clouds and red sequence. We have also plotted the optical TDEs (van Velzen et al. 2020) for comparison (green squares), in which the magnitudes are from either SDSS or PanSTARRS.

(close to the median redshift of our sample) using the IDL code KCORRECT (v4.3)<sup>7</sup> given by Blanton & Roweis (2007) (see also Blanton et al. 2003). To divide the SDSS galaxy sample into the red and blue class, we used the following magnitude-dependent color cut:

$$g-r = -0.027 * M_r + 0.14 \quad (7)$$

Our sample concentrates on the densest region of the CMD diagram (see Figure 11). There are 82 galaxies categorized into the red sequence and the fraction (59.9%) is somewhat comparable to the ensemble SDSS spectroscopic galaxy sample (63.0%). The difference in  $M_r$  is also tiny, with our sample only 0.24 magnitude brighter. In other words, the host galaxies of the MIR outburst are not significantly biased in terms of optical color and magnitudes. For comparison, the host galaxies of optically-selected TDE are much less luminous and most are dwarf galaxies.

<sup>7</sup> <http://kcorrect.org/>

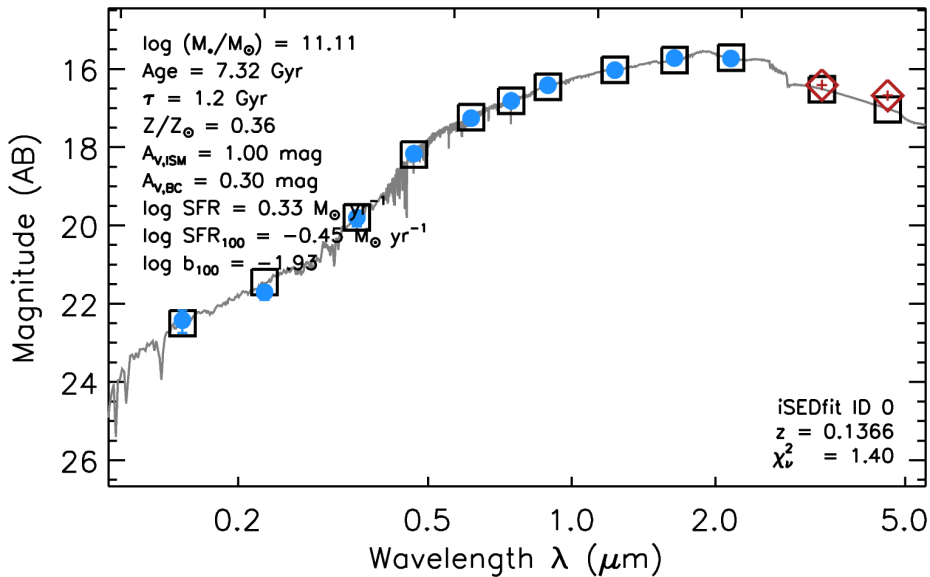


**Figure 12.** The SED fit of one galaxy (SDSSJ0000+1438) in our sample. We have collected the NUV (GALEX), optical (SDSS), NIR (UKIDSS or 2MASS) and MIR (*WISE*) magnitudes and then performed the fitting with `iSEDfit`. The blue filled circles are actual photometry data used in the fitting and the black open squares are predictions of the fitting model at the input bands. The *WISE* W1 and W2 bands (red open diamonds) have not been used in the fitting but only plotted as a comparison since the PSF magnitudes will underestimate the flux of extended sources (e.g., nearby galaxies). Most of the photometry errors are tiny and thus are not visible in the plots.

The SDSS data release provides also value-added catalog of the galaxy intrinsic properties<sup>8</sup>. For instance, the Portsmouth group has performed stellar kinematics and emission-line flux measurements (Thomas et al. 2013) using the publicly available codes Penalized PiXel Fitting (pPXF, Cappellari & Emsellem 2004) and Gas and Absorption Line Fitting (GANDALF v1.5; Sarzi et al. 2006). GANDALF fits stellar population and Gaussian emission line templates to the galaxy spectrum simultaneously to separate stellar continuum and absorption lines from the ionized gas emission. Stellar kinematics are evaluated by pPXF where the line-of-sight velocity distribution is fitted directly in pixel space. The fits account for the impact of diffuse dust in the galaxy on the spectral shape adopting a Calzetti (2001) extinction curve. Outputs from this fitting process include stellar velocity dispersions ( $\sigma_*$ ), emission-line fluxes, equivalent widths and BPT classifications. Note that for one source, SDSSJ1422+1609, the galaxy parameters are not available in the catalog due to the lack of SDSS spectrum.

The Portsmouth group has also provided the measurements of stellar mass ( $M_*$ ) through SED fitting with stellar population models (Maraston et al. 2013). However, their fittings only considered the SDSS optical photometry and may induce bias due to the narrow range of wavelength coverage. Therefore, we tried more comprehensive SED fittings by including the near IR and ultraviolet (UV) photometry, which is capable to better trace the old and young stellar populations,

respectively. The UV data are taken by the *Galaxy Evolution Explorer* (GALEX; Martin et al. 2005) with the near-UV (NUV) and far-UV (FUV) filters. For the NIR data, we adopted the *J, H, K*-band Petrosian magnitudes given by the UKIRT InfraRed Deep Sky Surveys (UKIDSS; Lawrence et al. 2007). For sources that are located outside the UKIDSS footprint, we used the magnitudes from the Two Micron All Sky Survey (2MASS; Skrutskie et al. 2006).

After gathering the UV, optical and NIR magnitudes as well as their errors, we begin the broadband SED fitting utilizing `iSEDfit`<sup>9</sup>, which is a code to determine the  $M_*$ , SFRs, and other physical properties of galaxies within a simplified Bayesian framework (Moustakas et al. 2013). The fitting results are quite good (see an example in Figure 12) and the resulted  $M_*$  are higher than those given by Portsmouth group by a median of 0.16 dex, indicating a fraction of old stellar population probably missed by the SED fitting using only the optical data. Generally, the  $M_*$  distribution is consistent with the  $M_r$ . Most galaxies (92.0%) have stellar masses in the range  $10^{10-11.5} M_\odot$  (median  $10^{10.7} M_\odot$ , see Figure 15). The least massive five galaxies with a mass lower than  $10^{9.5} M_\odot$  including the four SNe hosts, could be classified as dwarf galaxies since their masses are even lower than the Large Magellanic Cloud ( $2.7 \times 10^9 M_\odot$ , van der van der Marel et al. 2002).

## 5.2. Nuclear Activity and Mass of SMBHs

<sup>8</sup> <https://www.sdss.org/dr15/spectro/galaxy/>

<sup>9</sup> <http://www.sos.siena.edu/jmoustakas/isedfit/>

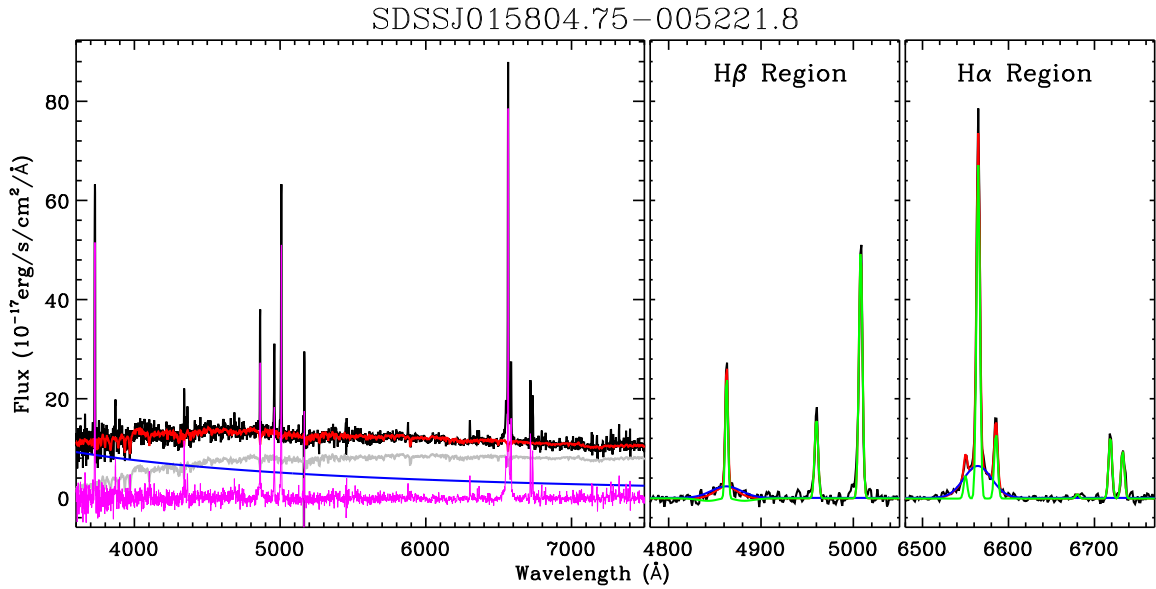


**Figure 13.** We show the analysis of the SDSS spectrum of SDSSJ0158-0052 as an illustration of the spectral decomposition. The left panel displays the subtraction of starlight (grey) and AGN continuum (blue). The sum of the starlight and continuum is plotted in red and the residual is plotted in magenta. The middle panel highlights the Gaussian fitting of H $\beta$ -[O III] region, in which the broad H $\alpha$  component, narrow lines and total are shown in blue, green and red respectively. The right panel is similar but for H $\alpha$ -[N II]-[S II] region.

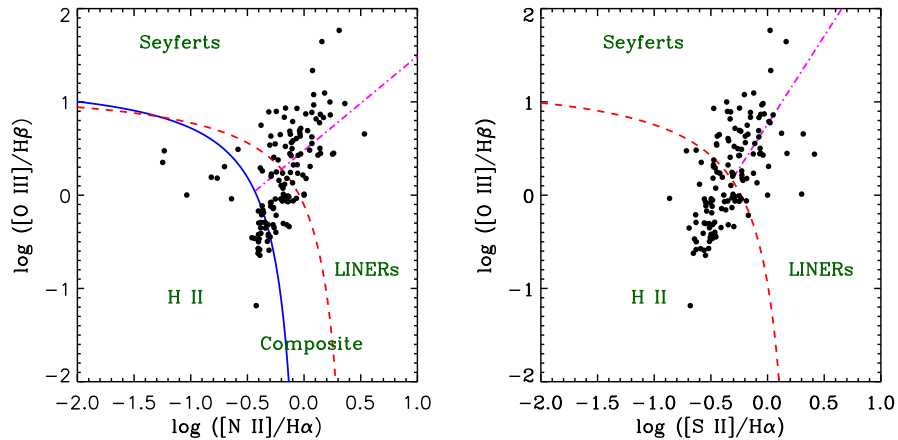


**Figure 14.** The locations of the MIR outburst galaxies (black filled circles) in the BPT diagram. The lines separating the different regions are mainly drawn from Kewley et al. (2006) only with the Seyfert/LINER dividing line (magenta dashed line) in the left panel from Cid Fernandes et al. (2010).

As we have mentioned in §1, the transient accretion onto SMBHs is a major population of extragalactic transients associated with galaxies. It is thus useful to assess the pre-outburst nuclear activity of these galaxies, which may shed light on the nature of the outburst. The narrow-line ratios of galaxies, namely their location at the BPT diagram, can be used as a diagnosis of the nuclear activity, but only the broad emission lines can give unambiguous evidence of active SMBHs and plausible estimated  $M_{\text{BH}}$ . In order to detect the potential broad lines, we have performed careful spectral analysis on the SDSS spectrum of these galaxies.

Our spectral fitting procedures are as follows: (1) subtracting the starlight and AGN continuum to obtain the emission-line residuals; (2) Gaussian fitting to emission lines including broad components when necessary. The spectrum is corrected for the Galactic extinction with the extinction map of Schlegel et al. (1998) and the reddening curve of Fitzpatrick (1999). We model the starlight component with the stellar templates of Lu et al. (2006), which were built from the simple stellar population spectra (Bruzual & Charlot 2003). The AGN continuum is modeled as a power law. After subtracting the starlight and AGN continuum component, we try to fit emission lines with multiple Gaussians while only broad

components ( $\sigma > 500 \text{ km s}^{-1}$ ) for  $\text{H}\alpha$ ,  $\text{H}\beta$ ,  $\text{Mg II}$  and  $\text{He I}$  are allowed to vary. Although emission lines in a fraction of galaxies can be fitted with a broad  $\text{H}\alpha$  component superimposed on the narrow component, only those broad  $\text{H}\alpha$  lines with S/N higher than 10 are considered as valid, resulting in a final sample of 26 galaxies. The robustness of our fitting results is demonstrated in SDSSJ0158-0052 (see Figure 13), which is a well-known low-mass AGN candidate selected by broad  $\text{H}\alpha$  emission (Greene & Ho 2007; Xiao et al. 2011). The  $M_{\text{BH}}$  is subsequently calculated by empirical virial mass estimator ( $M_{\text{BH}} = fRv^2/G$ ) for single-epoch spectra using the formalism presented in Greene & Ho (2007). This method postulates that the broad-line region (BLR) gas is virialized with velocity dispersion characterized by the widths of broad lines and a distance to the BH estimated from the conventional radius-luminosity relation (e.g., Kaspi et al. 2005; Bentz et al. 2013).

Regarding the narrow-line sources, their nuclear activity can be alternatively identified by their positions in the BPT diagram (see Figure 14). According to the classification of Portsmouth group (with the broad-line AGNs updated from our own fittings), our sample can be categorized into 37 (14 with broad lines) Seyferts, 23(4) LINERs, 35(2) starforming galaxies and 41(6) composites. Broad-line starforming galaxies are not common but indeed exist (see Figure 8 of Liu et al. 2019). However, the fraction in our sample looks somewhat high (2/35), which may indicate some of the MIR outburst in starforming galaxies are driven by AGNs. The total number of AGNs contained in our sample is 49 (37+4+2+6) when taking count of both Seyferts and broad-line sources in other BPT types. No clear evidence of intense AGN activity is found for other sources. We caution that LINERs can be treated as weak AGNs powered by SMBHs. In the absence of broad-lines, we have to estimate their  $M_{\text{BH}}$  with other approaches, such as the correlations with either the  $\sigma_*$  or mass of galactic bulge ( $M_{\text{bulge}}$ ) established in local massive galaxies (see Kormendy & Ho 2013 for a review). Our experiences and other works suggest that the velocity dispersion after correction of the instrument broadening ( $70 \text{ km s}^{-1}$ ) is reliable down to  $\sim 50\text{--}60 \text{ km s}^{-1}$  (e.g., Zahid et al. 2016; Chilingarian et al. 2017). Hence we adopted only the  $M_{\text{BH}}\text{--}\sigma_*$  relation when  $\sigma_* > 50 \text{ km s}^{-1}$ , leaving seven galaxies without  $M_{\text{BH}}$  measurements because of low  $\sigma_*$ . Although the  $M_{\text{BH}}\text{--}M_{\text{bulge}}$  relation (e.g., McConnell & Ma 2013) has been extensively used to estimate  $M_{\text{BH}}$ , the SDSS resolution is generally too low to isolate the bulge component from disk. We thus used the relation between  $M_{\text{BH}}$  and total stellar mass (Reines & Volonteri 2015) for the last seven objects. Our final sample has a broad range of  $M_{\text{BH}}$  with logarithmic mass from 4.5 to 9.0 (median 7.3, see Figure 15).

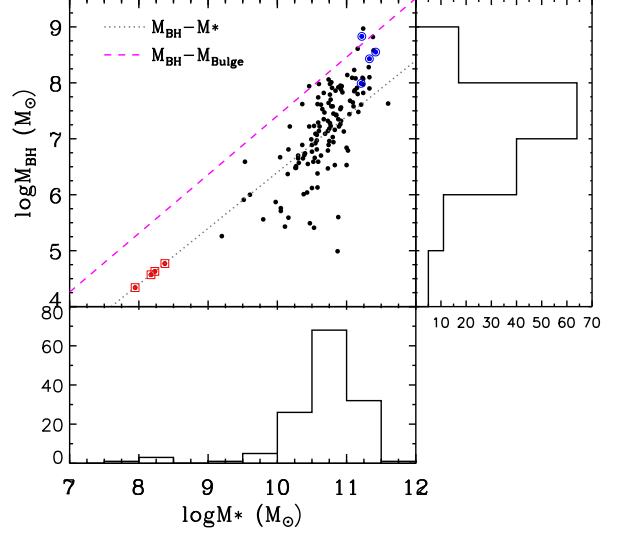


**Figure 15.** The black hole mass ( $M_{\text{BH}}$ ) versus stellar mass ( $M_*$ ) distribution of our sample. The red solid circles are SNe and the blue solid circles are strong jetted sources. The histogram of  $M_{\text{BH}}$  and  $M_*$  are shown in the right and bottom panels. Overlaid in grey dotted and magenta dashed lines are the correlation between  $M_{\text{BH}}$  and bulge mass (McConnell & Ma 2013) and total stellar mass (Reines & Volonteri 2015), respectively.

The above analysis of the properties of MIR flares and their host galaxies, allow us to explore further their physical nature. MIR flares can be generally attributed to non-thermal emission from jets or dust thermal emission heated by different processes, such as supernova, AGN or TDE. We will discuss each of these possibilities below.

### 6.1. Infrared Luminous Supernova

As mentioned in §3.1, SDSSJ0936+0615, SDSSJ1531+3724, SDSSJ1540+0054 and SDSSJ1554+1636 are known hosts of SNe reported by ASAS-SN<sup>10</sup>. Interestingly, their peak MIR luminosity appears to be lowest, with absolute W2 magnitudes fainter than  $-22$  (or  $\log L_{\text{W}2} < 42$ ). The reason for them to pass our selection threshold of variability amplitude ( $> 0.5 \text{ mag}$ ) could be the dwarfness of their host galaxies (see Figure 11), which makes the MIR outburst luminosity over luminous with respect to their host. Indeed, the four SNe galaxies are the least massive ones and occupy the low-mass end ( $\log M_* < 9$ ). In addition, these galaxies appear very young in terms of their blue colors ( $g-r < 0.5$ ). Hence, the SNe in our sample, in a word, occupy the lowest MIR luminosity end, and reside in dwarf starforming galaxies.

The spectroscopic follow-ups have classified the four SNe into three type II and one Ia-91T like sources. Previous stud-

<sup>10</sup> [http://www.astronomy.ohio-state.edu/asassn/sn\\_list.html](http://www.astronomy.ohio-state.edu/asassn/sn_list.html)



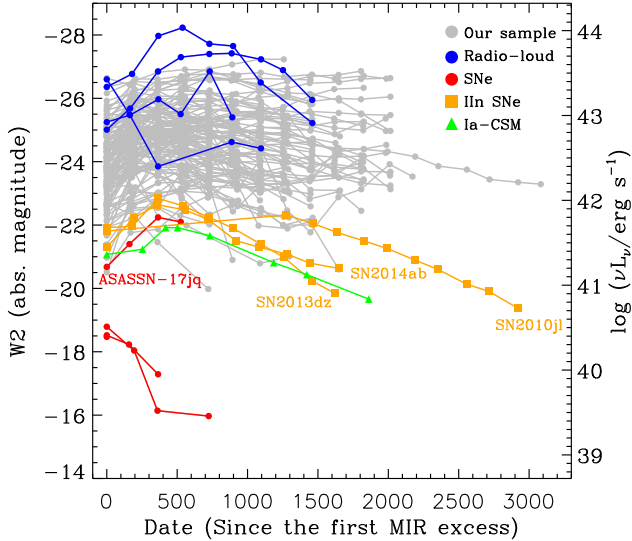


**Figure 16.** The time-resolved W2 magnitudes with date zeropoint set as the time of first MIR excess. Our sample has been plotted in solid grey circles with the radio-loud sources and SNe highlighted in blue and red, respectively. We have also overplotted other IR luminous SNe (orange squares), which are among the brightest known to us, for comparison. The Ia-CSM light curve (green triangles) are drawn from Fox et al. (2013).

ies suggest that the IR emission of SNe IIn are statistically more luminous and long-lasting than other types (e.g., type Ia) due to the heating of preexisting dust in the circumstellar medium (CSM) (Fox et al. 2013; Tinyanont et al. 2016). The SNe Ia usually show very weak MIR emission and are not detectable in three years after the explosion (Tinyanont et al. 2016) except the Ia-CSM subclass. In the same way, some 91T-like SNe also display the interacting CSM (e.g., Harris et al. 2018), which could be responsible for the observed MIR flare. The luminous infrared transients uncovered by SPIRITS project are mainly obscured core-collapse SNe with peak  $4.5\mu\text{m}$  (*Spitzer*, roughly *WISE* W2) magnitudes between -14 and -18.2 (Jencson et al. 2019), which are significantly fainter than that in our sample.

The evolution of absolute W2 magnitudes as a function of time is presented in Figure 16. It is clear that the four SNe have the faintest MIR emission (see also the peak magnitude distribution in Figure 6) and their duration is relatively short. While the SNe occurred in SDSSJ1531+3724 (ASASSN-17jq) is relatively bright, it is still fainter than non-SNe objects. In our previous work (Jiang et al. 2019), we have checked for the *WISE* light curves of all SNe in the public catalog reported between 2008 and 2018. Among them, the most luminous ones are all IIn (e.g., SN2010jl, SN2013dz and SN2014ab) with luminosity  $L_{W2} \sim 10^{42} \text{ erg s}^{-1}$ , which is comparable to that of ASASSN-17jq. In summary, the MIR luminosity of our sample is systematically higher than SNe

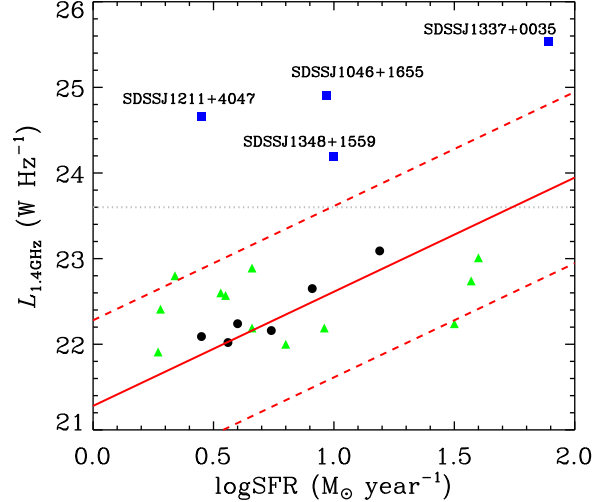


**Figure 17.** The 1.4 GHz luminosity versus the SFR of radio detected sources in our sample. The red line is the expected radio emission from star formation (Equation 3 in Davies et al. 2017). One index offset from the expectation are plotted as red dashed lines. We have highlighted the radio-loud AGNs with blue squares and other AGNs (Seyferts or broad  $H\alpha$  objects) with green triangles. The grey dotted line represents the radio luminosity beyond which can be considered as undisputed jet origin (Kellermann et al. 2016).

by at least 2-3 magnitudes, thus the SNe scenario is disfavored as the origin for the bulk of MIRONG.

## 6.2. Non-thermal emission from Jet

We next examine the possibility of non-thermal emission produced by relativistic jets. It has been proved that the synchrotron radiation of jets can contribute significantly to the MIR emission as well as its variability (e.g. Jiang et al. 2012; Liao et al. 2019). We cross-matched our sample with the catalog of Faint Images of the Radio Sky at Twenty cm (FIRST)<sup>11</sup> using a matching radius of  $5''$ , resulting in 22 objects detected with S/N higher than 5. There are eight objects outside of the FIRST footprint, so we matched them with the NRAO VLA Sky Survey (NVSS) catalog<sup>12</sup> but found non-detections.

The radio detections do not necessarily suggest the association with jet activity, since the star formation may also contribute to the radio emission. We used the star formation rate (SFR) given by Chang et al. (2015), which is derived by fitting the broadband SDSS+*WISE* SED using MAGPHYS (da Cunha et al. 2008). The SFR measurements for 128 out of 137 galaxies are found. For the remaining sources, the SFRs

<sup>11</sup> <http://sundog.stsci.edu/cgi-bin/searchfirst>

<sup>12</sup> <https://www.cv.nrao.edu/nvss/NVSSlist.shtml>

were estimated from the  $24\ \mu\text{m}$  flux<sup>13</sup> (Chary & Elbaz 2001). Then we calculated the expected radio flux from star formation using the correlation between 1.4 GHz luminosity ( $L_{1.4\text{G}}$ ) and SFR (Equation 3 in Davies et al. 2017). As displayed in Table 5 and Figure 17, the radio emission for star-forming and composite galaxies are fully consistent with the expectation from the star formation. Only SDSSJ1337+0035, which is a composite but shows extremely high radio power, is an exception. We then used the radio-loudness parameter  $R$  to quantify the radio intensity for AGN sources (Seyferts or LINERs) plus SDSSJ1337+0035, which is defined as the ratio of the flux densities between 6 cm and 4400 Å (Kellermann et al. 1989). Here the 6 cm flux is derived from the 1.4 GHz flux assuming a spectral slope  $-0.7$ . The 4400 Å flux is converted from the 5100 Å flux, which is derived from the bolometric luminosity ( $L_{\text{bol}}$ ). The latter is computed from the [O III] luminosity (Lamastra et al. 2009) assuming a bolometric correction of 8.1 (Runnoe et al. 2012). The derived radio-loudness parameters are listed in Table 5.

Four galaxies (SDSSJ1046+1655, SDSSJ1211+4047, SDSSJ1337+0035, SDSSJ1348+1559) stand out from the rest in above evaluations. They show radio power 38-600 times higher than that predicted from SFR. Meanwhile, their radio-loudness ( $>1000$ ) is at least two orders of magnitude higher than other sources. Moreover, the radio luminosity for the four sources is higher than  $10^{23.6}\ \text{W Hz}^{-1}$ , above which a radio-loud AGN can be classified (Kellermann et al. 2016). Therefore, they are likely radio-loud AGNs, for which the MIR flares could originate from the non-thermal emission of pre-existing jets. For those galaxies that are not radio-loud before the MIR flare, we cannot rule out the probability of a new-formed relativistic jet contributing the MIR emission. Unfortunately, no quasi-simultaneous radio observations are available. In fact, by examining the *WISE* light curves in each epoch, we did not find any evidence for intraday variability, which could indicate the presence of a relativistic jet (Jiang et al. 2012). Timely radio follow-ups would be helpful to further test this intriguing scenario.

### 6.3. Dust Echo of Transient SMBH Accretion

After removing the 4 known SNe and 4 radio-loud sources, we now investigate the origin of MIR outbursts for the other 129 galaxies in our sample. As we analyzed in §5.2, there are 49 galaxies that show evidence of AGN activity in their optical spectra. In addition, 16 galaxies can be classified as LINERs. Therefore, the 128 galaxies (except SDSSJ1422+0609 for which the SDSS spectrum is not available) can be grouped by two populations, including 65 AGNs (49 Seyferts and 16 LINERs) and 63 quiescent galaxies.

<sup>13</sup> Here we adopted the *WISE* W4 band ( $22\ \mu\text{m}$ ) flux as an approximation.

#### 6.3.1. Echoes of Turn-on AGNs

The UV/optical variability on various time scales are well known to be an inherent property of AGNs albeit the physical mechanism behind is not fully understood (Ulrich et al. 1997). The amplitude of optical variability is typically a few tenths of magnitudes within time-scale of months, but also showing larger variations over longer time-scales. There is an increasing population of dramatically variable AGNs, so-called CL AGNs, which exhibit flux rising/declining in continuum ( $\Delta m > 1\ \text{mag}$ ) over several years and change accordingly spectral types (e.g., LaMassa et al. 2015; Runnoe et al. 2016; MacLeod et al. 2016; Yang et al. 2018). Specifically, the CL AGNs with rising/declining photometric light curves are termed "turn-on"/"turn-off". In addition to state changes found in CL AGNs, major outbursts have also been found in AGNs (e.g., Graham et al. 2017; Trakhtenbrot et al. 2019).

In the AGN unification, the dusty torus is a vital ingredient to address a variety of phenomenons in different types of AGNs. The torus will unavoidably absorbs part of the UV-optical photons from the accretion disk and reprocesses them into the IR. The picture has been widely accepted through the spectral energy distribution (SED) fitting (e.g., Fritz et al. 2006; Nenkova et al. 2008; Stalevski et al. 2012) and IR reverberation mapping (e.g., Suganuma et al. 2006; Koshida et al. 2014; Lyu et al. 2019). It is plausible that our discovered MIR flares are due to dust echoes of turn-on AGNs. Such a scenario can be tested by obtaining new optical spectra to see whether there is evident spectral evolution. In fact, we have performed a detailed study of SDSSJ1115+0544, which has undergone a brightening by 2.5 mag in *V*-band over  $\sim 120$  days, then faded by 0.5 mag over 200 days, followed by a plateau lasting for  $> 600$  days. The multi-epoch optical spectra over 400 days in the plateau phase revealed newly formed and steady broad  $\text{H}\alpha$ ,  $\text{H}\beta$  emission, that is compatible with the characteristic of a turn-on AGN (Yan et al. 2019). Intriguingly, together with the three objects (SDSSJ1554+3629, SDSSJ0945+4814 and SDSSJ1133+6701) mentioned in §3.1, the four reported sources are all classified as LINERs in the BPT diagram, which may suggest a uniform class of turn-on system (Friederick et al. 2019).

#### 6.3.2. Echoes of Tidal Disruption Events

Nearly half objects in our sample show no signs of AGN activity, neither Seyfert nor LINER, in the SDSS spectra. The giant nuclear flares of inactive galaxies are usually attributed to TDEs. For Schwarzschild BHs, the TDEs are observable only when the BH masses are lower than the Hills mass ( $\sim 10^8 M_{\odot}$ ). Otherwise, the star will be swallowed wholly rather than produce an electromagnetically luminous flare because its tidal radius is within the horizon (Hills 1975; Rees 1988). The  $M_{\text{BH}}$  distribution of our sample peaks at  $2.0 \times 10^7 M_{\text{BH}}$

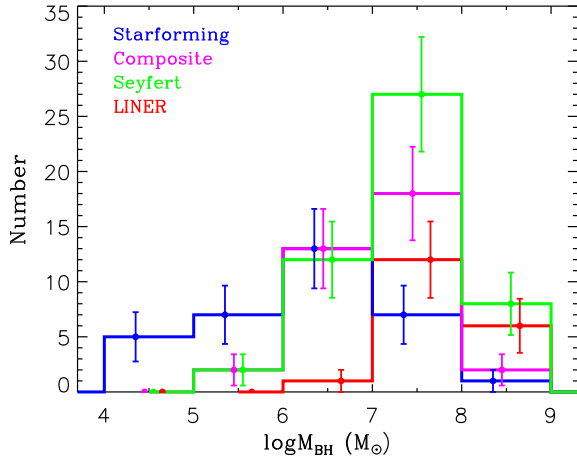


**Figure 18.** The histograms of  $M_{\text{BH}}$  for starforming (blue), composite (magenta), Seyfert (green) and LINER (red) galaxies in our sample as classified by the BPT diagram. The bars errors are the Poisson fluctuations of the number in each bin. Noting that we have put all broad-line sources into the ‘Seyfert’ subset whatever their BPT types are.

with only 17 (12.4%) greater than  $10^8 M_{\odot}$  (see Figure 15). If excluding Seyferts and LINERs, only three galaxies are more massive than the Hills mass (see Figure 18), hence the TDE interpretation for the MIR bursts is possible.

Similar to AGNs, the UV/optical photons released by TDEs can be absorbed by dust in the vicinity of BH and re-processed into the IR band, giving rise to an IR flare like an echo. Lu et al. (2016) have calculated the light curve of the IR echo with 1-D radiative transfer model and showed that the dust emission peaks at MIR (3-10  $\mu\text{m}$ ). They have predicted that the typical luminosity is between  $10^{42}$  and  $10^{43}$   $\text{erg s}^{-1}$ , depending on the dust covering factor (ranging from 0.1 to 1), which is fairly comparable with that inferred in our sample. Such an IR echo has been detected in a handful of optical TDEs from the *WISE* data, (Jiang et al. 2016; van Velzen et al. 2016) though the amplitude of IR variability is smaller ( $\sim 0.2$  mag) compared with the sample in this work. Furthermore, Dou et al. (2016) have reported the long-lasting IR echoes from four coronal-line TDE candidates (Wang et al. 2012; Yang et al. 2013). These findings suggest that IR echoes might be ubiquitous for TDEs occurred in gas (dust)-rich nuclear environment.

On the other hand, the IR echo itself is suggestive of TDEs in dust-rich environment. Wang et al. (2018) have conducted a systematical search and obtained a sample of 19 low-redshift ( $z < 0.22$ ) non-Seyfert galaxies that display slow decline in the MIR emission, reminiscent of those coronal-line TDEs (Dou et al. 2016). Unfortunately, because they are already in the late fading stage, the spectroscopic observations might be too late to identify the TDE-like characteristics. In contrast, our objects are observed at much earlier

phase, either still rising or just decaying, which are valuable for timely multi-wavelength follow-ups. By checking for optical counterparts (see §3.1), we found that SDSSJ0158-0052 (PS16dtm) and SDSSJ1620+2407 (ATLAS17jrp) have been indeed alerted as TDE candidates (Blanchard et al. 2017; Fraser et al. 2017). The identifications of TDEs in our sample are thus encouraged. We caution that even for active galaxies in our sample, the TDE scenario is possible and worthwhile to explore. One universal manifestation accompanied with AGN TDEs (e.g., Tadhunter et al. 2017; Blanchard et al. 2017; Kankare et al. 2017) is long-lasting and luminous MIR flares as a result of echoes of dusty torus (Dou et al. 2017; Jiang et al. 2017, 2019).

Given the faintness in the optical bands for most MIRONGs (§3.1), they could be promising candidates of dust-obscured TDEs that are still poorly explored. If not due to obscuration, their optical emission should be otherwise intrinsically weak, which is especially possible in the TDE scenario. The electromagnetic output of TDEs was initially thought to be dominated by X-ray or FUV emission from accretion, making the origin of optical emission remains hotly disputed (Roth et al. 2020). Therefore, some objects in our sample could belong to classical TDEs, which are luminous in X-ray/FUV but are faint in optical band. In this sense, the IR search of TDEs is superior to other individual bands as long as the BH is set in dusty environment.

Based on the sample of 19 galaxies, Wang et al. (2018) have found that the peak MIR luminosity is well correlated with the  $M_{\text{BH}}$ . However, the correlation (excluding SNe) appears less significant in our sample presented here (see Figure 19), though a Spearman rank analysis gives a correlation coefficient of  $\rho = 0.377$ , corresponding to a null hypothesis probability of  $p = 8 \times 10^{-6}$ . If we examine the dust mass instead of luminosity, the correlation is even less obvious ( $\rho = 0.116$ ,  $p = 0.001$ ).

## 7. DISCUSSION

Similar to Wang et al. (2018), our tentative conclusion is that the MIRONGs discovered by us are most likely associated with transient SMBH accretion, either in the form of TDE or turn-on AGN activity. Only a small fraction of them are due to IR-luminous SNe or non-thermal emission from relativistic jets. The conclusions are supported by several lines of evidence: 1) the outburst locations prefer to be in the region very close to the galactic center; 2) the maximum MIR luminosity is higher than the brightest SNe by 1-2 orders; 3) only few have radio-loud jet emission before the outburst; 4) the luminosity function broadly agrees with results of optical and X-ray TDEs (or nuclear transients).

In order to differentiate the diverse nature of these MIRONG, multi-wavelength follow-up observations have been conducted, including optical spectra (Y. B. Wang et al.

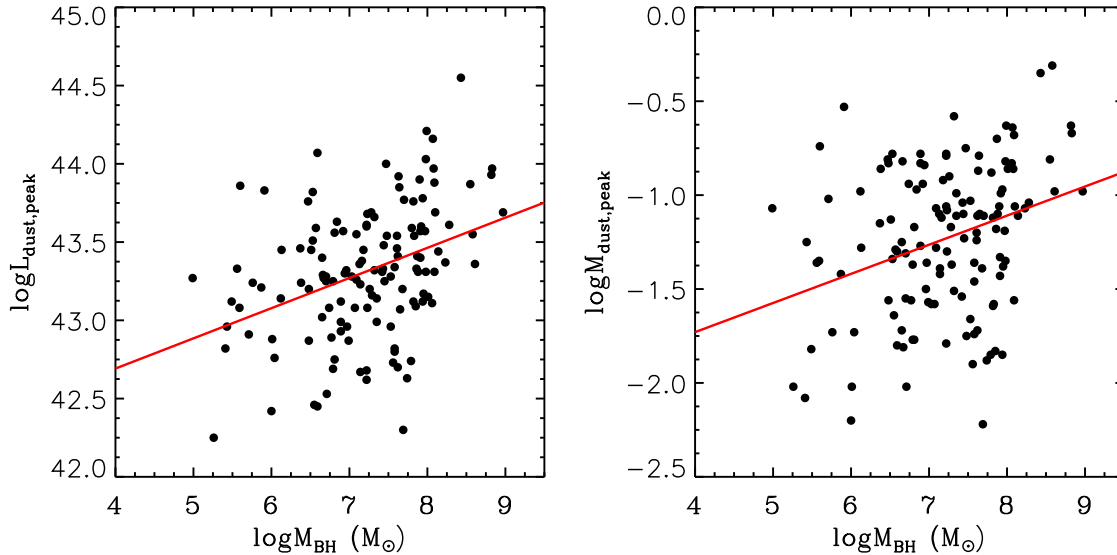


**Figure 19.** Left panel: the correlation between peak MIR luminosity ( $L_d$ ) and  $M_{\text{BH}}$ . Right panel: the correlation between the inferred dust mass ( $M_d$ ) and  $M_{\text{BH}}$ . Overlaid in red are the linear least-squares fitting. The  $L_d$  and  $M_d$  values are derived by dust with absorption efficiency (see Table 2).

in preparation), NIR photometry (H. Liu et al. in preparation), radio (Dai et al. 2020) and X-ray observations. So far, we have successfully obtained a sizable sample of likely TDEs or turn-on AGNs, which will be reported in the following series of papers. These events are generally not detected in the optical band and thus largely overlooked by previous works, hence present a significant advance over previous studies of similar events.

### 7.1. TDE Demography and Missing Energy Puzzle

The observations of TDEs are initially restricted to the serendipitous discoveries of X-ray flares in the centers of galaxies, yielding a very limited number of candidates. The number has grown remarkably in the past decade with the advent of dedicated optical time-domain surveys (Komossa 2015; van Velzen et al. 2020). However, there is still a large discrepancy in the event rate between observation and theory (Stone et al. 2020). The observations usually find a rate of  $\sim 10^{-5} \text{ gal}^{-1} \text{ yr}^{-1}$  (Donley et al. 2002; van Velzen & Farrar 2014), which is at least an order of magnitude below the theoretical estimation in realistic galactic nuclei (Wang & Merritt 2004; Stone & Metzger 2016). Although dynamical mechanisms to suppress TDE rates have been proposed, they seem unlikely to work in practice (e.g. Lezhnin & Vasiliev 2015). One solution may be a very broad intrinsic TDE luminosity function of which we have so far only seen the high end at given band (e.g., Blagorodnova et al. 2017; van Velzen 2018) in view of the complicated radiative emission mechanisms (Roth et al. 2020). The TDE demography at any single band can be thus seriously underestimated.

Moreover, the rate discrepancy becomes more specific and definitive when optical TDEs are found being overrepresented in post-starburst (or so-called E+A) galaxies with the rate elevated by a factor of  $\sim 100$  (e.g. Arcavi et al. 2014; French et al. 2016). This preference can not be fully accounted for by selection effects in comparison with control samples (Law-Smith et al. 2017). Such an enhancement is difficult to understand in theory, even though their hosts show high central stellar densities (French et al. 2020). This would require violent dynamical processes to occur but it seems impossible in most post-starburst galaxies.

Another observational discrepancy is known as the missing energy puzzle, namely a huge shortage of the observed energy relative to predictions. In the simplest picture, if half stellar material is accreted onto the BH, the expected energy released is  $\sim 10^{52} - 10^{53}$  erg. The observed total energy of optical TDEs is only  $\sim 10^{51}$  erg. Where is the missing 90–99% of the energy? Some models argue that the real accretion efficiency is actually quite low due to advection or outflow (e.g., Svirski et al. 2017; Dai et al. 2018). Lu & Kumar (2018) suggest that the missing part may be in the unobserved extreme-UV (EUV) band and/or in the form of relativistic jets. The jet mode is disfavored as the rareness of jetted TDEs but the EUV option coincides with the theoretical peak and the Rayleigh-Jeans-like optical/NUV SED. If that is true, at least in several TDEs, the issue then goes to how to measure the EUV energy which is invisible directly.

Two recent studies may shed light on an avenue to solve or alleviate the puzzles above. Tadhunter et al. (2017) has reported a candidate TDE in F01004-2237 from a sample of 15 nearby ultra-luminous infrared galaxies (ULIRGs), suggest-



ing an event rate as high as  $\sim 10^{-2} \text{ gal}^{-1} \text{ yr}^{-1}$ . The ULIRGs are generally starburst systems with a large amount of dust which is able to even veil energetic outbursts like TDEs. In the meantime, the energy absorbed by dust will manifest the original TDE emission as a luminous IR echo. The picture is nicely corroborated by the huge MIR flare detected in F01004-2237 (Dou et al. 2017), whose integrated IR energy till now is  $> 3 \times 10^{52} \text{ erg}$ . The other work claims a dust-enshrouded TDE in the western nucleus (B) of the merging galaxy pair Arp 299 (Mattila et al. 2018). This event is almost silent in optical and X-ray, but displays long-lasting echoes in the NIR and MIR with a total radiated energy  $> 1.5 \times 10^{52} \text{ erg}$ . The missing energy puzzle is almost settled in both systems when the IR energy is taken into account.

The two case studies also hint that perhaps the TDEs in post-starburst systems are only the tip of the iceberg and the real TDE rate in starburst galaxies could be immense (Guillochon 2017). It is widely believed that the galaxy mergers or interactions are capable of driving galactic-scale gas inflow to the nuclear region and triggering intense star formation. Even for an isolated disk galaxy, its center could be a concentrated region of gas and dust ornamented by enhanced star formation. Indeed, a considerable fraction of galaxies in the MIRONG sample are starforming systems as indicated by their SDSS fiber spectrum, whose nucleus are easily obscured as a result of intense star formation process.

Interestingly, the MIRONG event rate estimated by us is  $5.4 \times 10^{-5} \text{ gal}^{-1} \text{ yr}^{-1}$  (see §4.1), which is comparable to that of optical TDEs. It would be of a high value if a large percentage of them are eventually confirmed as real TDEs. Furthermore, if we naively assume a typical dust covering factor as AGN torus, the inferred luminosity function of the MIRONG is comparable with the observations of X-ray (Auchettl et al. 2018) and optical TDEs (van Velzen 2018) at high end (see Figure 10). The faint-end discrepancy is at least partly caused by the imperfect correction for the sample completeness of various selection approaches. We emphasize again that our selection criteria is somewhat strict ( $>0.5 \text{ mag}$  brightening). In the future we will extend the sample by a relaxed requirement to obtain a more complete view of the event rate and the luminosity function at faint end. The new population that is largely missed by optical surveys, due to either dust obscuration or intrinsically faintness, may offer us a promising approach to solve the problems of TDE demographics and missing energy.

### 7.2. Implication on the Turn-on and Duty Cycle of AGNs

CL AGNs have gradually become a rather popular phenomenon. The early searching has been focused mainly on known quasars, which naturally yield out more "turn-off" AGNs. The systematical discovery of "turn-on" cases have to start from a much larger galaxy sample, consisting

of both Seyfert and normal galaxies. Galaxies which show rapid transformation from a quiescent galaxy to a type 1 AGN within several months to years are of great interest. So far, only two unambiguous systems (iPTF 16bco and SDSSJ1115+0544) have been reported (Gezari et al. 2017; Yan et al. 2019). We refer them to *bona fide* turn-on AGNs, which are different from the normal CL AGNs that usually changed from type 2/1.9/1.8 to type 1. Some CL AGNs have shown to change their types back and forth frequently (e.g., Denney et al. 2014; McElroy et al. 2016; Oknyansky et al. 2019), implying the existence of a persistent but unstable accretion disk, e.g., susceptible and sensitive to gas feeding. In comparison, the *bona fide* turn-on AGNs can serve as a more genuine laboratory than normal CL AGNs to explore the ignition mechanism of SMBHs, e.g., the rapid formation of accretion disk as well as the origin of concomitant multi-wavelength emission (e.g., X-ray, radio).

It is worthwhile to note that both iPTF 16bco and SDSSJ1115+0544 are present in our MIRONG sample. It suggests that more similar systems would present in our sample in view of the quiescence of many galaxies before the outburst, and the selection of "turn-on" AGNs might be effectively using the MIR light curves. The dust covering factors ( $f_d$ ) of quiescent SMBHs are around  $10^{-2}$  as revealed by the IR echoes of optical TDEs, which is at least one order of magnitude lower than that in AGNs (van Velzen et al. 2016; Jiang et al. 2020). We estimated the  $f_d$  of turn-on AGNs with the similar method used in Jiang et al. (2020), which is  $f_d = L_{\text{dust}}/L_{\text{bol}}$ . The  $L_{\text{bol}}$  of iPTF 16bco and SDSSJ1115+0544 after state transformation are  $\sim 10^{45} \text{ erg s}^{-1}$  (Gezari et al. 2017) is  $\sim 4 \times 10^{44} \text{ erg s}^{-1}$  (Yan et al. 2019), respectively. Meanwhile, their peak dust luminosity ( $L_{\text{dust}}$ ) inferred from WISE W1 and W2 photometry (fitted by a blackbody radiation) is  $\sim 10^{44} \text{ erg s}^{-1}$  and  $3 \times 10^{43} \text{ erg s}^{-1}$ , respectively. The inferred  $f_d$  ( $\sim 0.1$ ) for "turn-on" AGNs appears to fall within the regime connecting normal galaxies and AGNs. The result is interesting, and may shed important light onto the triggering mechanism of AGNs, which is perhaps regulated by the availability of interstellar medium in the vicinity of SMBHs.

If "turn-on" AGNs occur only when a large amount of gas and dust accumulate around the SMBHs, the dust echo appears inevitable, explaining the high efficiency of searching in MIR. Particularly in the extremely dusty environments, the ignited SMBHs can be severely obscured and only be identified in the IR (§7.1). Uncovering more *bona fide* turn-on AGNs are valuable not only for understanding the AGN accretion physics, but also for the probe of AGN duty cycle as well as the impact on their host galaxies. The duty cycle, namely the accreting phase of a SMBH (i.e., AGN phase) is considered to be roughly a few times  $10^7 \text{ yr}$  (Combes et al. 2000; Haehnelt & Rees 1993). However, the turn-on time scale is found within one year (Gezari et al. 2017; Yan et



al. 2019), indicating that the event rate could be as low as  $\sim 10^{-7}$ . Such a low expected rate seems contrary to the discovery of two and possibly more cases in our sample. Perhaps the traditional duty cycle of  $10^7$  yr is only suitable for the total active time but not appropriate for flare events which may have different time scales. The current and future surveys may be able to constrain the time scale distribution with a large number of newly discovered "turn-on" AGNs. The specific mode of AGN duty cycle may have distinctive influence on their host galaxies and advance our understanding of galaxy evolution.

## 8. SUMMARY AND PROSPECTS

The combined *WISE* and *NEOWISE* light curves, which have a time baseline of about one decade with a cadence of half year, have provided us a unique dataset for MIR time-domain study. Starting from  $\sim 1$  million SDSS galaxies, we have selected out 137 galaxies which have displayed MIR outburst with amplitude  $> 0.5$  magnitude with respect to the pre-outburst quiescent phase. Only a small fraction (15/137) of these outbursts have been reported by optical surveys including four SNe, two TDE candidates, three turn-on AGNs and six unclassified objects. The remaining sources are likely associated with the dust echoes of transient accretion events of SMBHs, as suggested by their proximity to host galaxy centers, their high MIR luminosity, weak radio emission and MIR luminosity distribution, *i.e.* luminosity function. We are undertaking multi-wavelength follow-up observations to identify the nature of these MIR outburst in nearby galaxies (MIRONG). The MIRONG unveiled by our study demonstrate the importance and necessity of MIR time-domain survey. For example, they may pave a way to solve the perplexed issues in the current study of TDEs and changing-look AGNs.

Since the *NEOWISE* survey is on-going, we expect more data points will be accumulated in the future. Additional data will help us diagnose the nature of MIR outbursts and obtain better measurements of dust properties. In addition, more MIR transients will be discovered with the updated database. At the post-*WISE* era, the Near-Earth Object Camera (NEOCam) is a planned mission to discover and

characterize asteroids and comets at two MIR channels simultaneously, which will cover 68% of the extragalactic sky at the wavelengths of  $4.0\text{--}5.2\ \mu\text{m}$  and  $6.0\text{--}10.0\ \mu\text{m}$ , respectively (Ross et al. 2019). The survey depth of NEOCam is quite similar to *NEOWISE* yet its cadence is even better with on average 30 visits per year. Moreover, the already selected SPHEREx mission (Doré et al. 2016) that is scheduled to launch in 2023, will be an excellent complement to NEOCam at near-IR band, aiming to obtain spectra over  $0.75\text{--}5\ \mu\text{m}$  across the full sky. It will scan the entire sky four times during its nominal 25-month mission life, though it is not as deep as *WISE*. Therefore, the prospects for the study of MIR transients are still very bright.

We are grateful to the anonymous referee for his/her careful reading and nice comments, which have greatly improved the paper. We thank Dr. Roc Cutri for many useful suggestions about the use of *WISE* and *NEOWISE* archival data all the time and Dr. John Moustakas for his nice help for the usage of IDL/*iSEDfit*. This work is supported by the Chinese Science Foundation (NSFC-11833007, 12073025, 11421303, 11733001), Joint Research Fund in Astronomy (U1731104) under cooperative agreement between the NSFC and the CAS, Anhui Provincial Natural Science Foundation and the Fundamental Research Funds for the Central Universities. This research makes use of data products from the *Wide-field Infrared Survey Explorer*, which is a joint project of the University of California, Los Angeles, and the Jet Propulsion Laboratory/California Institute of Technology, funded by the National Aeronautics and Space Administration. This research also makes use of data products from *NEOWISE-R*, which is a project of the Jet Propulsion Laboratory/California Institute of Technology, funded by the Planetary Science Division of the National Aeronautics and Space Administration. This research has made use of the NASA/IPAC Infrared Science Archive, which is operated by the California Institute of Technology, under contract with the National Aeronautics and Space Administration. This research has made use of the NASA/IPAC Extragalactic Database (NED), which is operated by the Jet Propulsion Laboratory, California Institute of Technology, under contract with the National Aeronautics and Space Administration.

## REFERENCES

- Abolfathi, B., Aguado, D. S., Aguilar, G., et al. 2018, *ApJS*, 235, 42  
 Alexander, K. D., Berger, E., Guillochon, J., Zauderer, B. A., & Williams, P. K. G. 2016, *ApJL*, 819, L25  
 Arcavi, I., Gal-Yam, A., Sullivan, M., et al. 2014, *ApJ*, 793, 38  
 Arcavi, I., Howell, D. A., Kasen, D., et al. 2017, *Nature*, 551, 210  
 Assef, R. J., Prieto, J. L., Stern, D., et al. 2018, *ApJ*, 866, 26  
 Auchettl, K., Ramirez-Ruiz, E., & Guillochon, J. 2018, *ApJ*, 852, 37  
 Baldwin, J. A., Phillips, M. M., & Terlevich, R. 1981, *PASP*, 93, 5  
 Barvainis, R. 1987, *ApJ*, 320, 537  
 Bell, E. F., Wolf, C., Meisenheimer, K., et al. 2004, *ApJ*, 608, 752  
 Bender, P. L. 1998, *Eighteenth Texas Symposium on Relativistic Astrophysics*, 536  
 Bentz, M. C., Denney, K. D., Grier, C. J., et al. 2013, *ApJ*, 767, 149  
 Blagorodnova, N., Gezari, S., Hung, T., et al. 2017, *ApJ*, 844, 46  
 Blanchard, P. K., Nicholl, M., Berger, E., et al. 2017, *ApJ*, 843, 106  
 Blanton, M. R., Brinkmann, J., Csabai, I., et al. 2003, *AJ*, 125, 2348  
 Blanton, M. R., & Roweis, S. 2007, *AJ*, 133, 734  
 Bloom, J. S., Giannios, D., Metzger, B. D., et al. 2011, *Science*, 333, 203  
 Bruzual, G., & Charlot, S. 2003, *MNRAS*, 344, 1000  
 Burrows, D. N., Kennea, J. A., Ghisellini, G., et al. 2011, *Nature*, 476, 421  
 Calzetti, D. 2001, *PASP*, 113, 1449  
 Cappellari, M., & Emsellem, E. 2004, *PASP*, 116, 138  
 Chambers, K. C., Magnier, E. A., Metcalfe, N., 2016, arxiv:1612.05560

- Chang, Y.-Y., van der Wel, A., da Cunha, E., et al. 2015, *ApJS*, 219, 8
- Chary, R., & Elbaz, D. 2001, *ApJ*, 556, 562
- Chilingarian, I. V., Zolotukhin, I. Y., Katkov, I. Y., et al. 2017, *ApJS*, 228, 14
- Cid Fernandes, R., Stasińska, G., Schlickmann, M. S., et al. 2010, *MNRAS*, 403, 1036
- Combes, F., Mamon, G. A., & Charmandaris, V. 2000, *Dynamics of Galaxies: From the Early Universe to the Present*
- da Cunha, E., Charlot, S., & Elbaz, D. 2008, *MNRAS*, 388, 1595
- Dai, B. B., Shu, X. W., Jiang, N., et al. 2020, *ApJL*, 896, L27
- Dai, L., McKinney, J. C., Roth, N., et al. 2018, *ApJL*, 859, L20
- Davies, L. J. M., Huynh, M. T., Hopkins, A. M., et al. 2017, *MNRAS*, 466, 2312
- Denney, K. D., De Rosa, G., Croxall, K., et al. 2014, *ApJ*, 796, 134
- Dong, S., Shappee, B. J., Prieto, J. L., et al. 2016, *Science*, 351, 257
- Donley, J. L., Brandt, W. N., Eracleous, M., & Boller, T. 2002, *AJ*, 124, 1308
- Doré, O., Werner, M. W., Ashby, M., et al. 2016, *arXiv:1606.07039*
- Dou, L., Wang, T., Jiang, N., et al. 2016, *ApJ*, 832, 188
- Dou, L., Wang, T., Yan, L., et al. 2017, *ApJL*, 841, L8
- Draine, B. T., & Lee, H. M. 1984, *ApJ*, 285, 89
- Drake, A. J., Djorgovski, S. G., Mahabal, A., et al., 2009, *ApJ*, 696, 870
- Drake, A. J., Djorgovski, S. G., Graham, M. J., *MNRAS*, 482, 98
- Eales, S. 1993, *ApJ*, 404, 51
- Evans, C. R., & Kochanek, C. S. 1989, *ApJL*, 346, L13
- Fitzpatrick, E. L. 1999, *PASP*, 111, 63
- Fox, O. D., Filippenko, A. V., Skrutskie, M. F., et al. 2013, *AJ*, 146, 2
- Fraser, M., Rybicki, K., Gromadzki, M., et al. 2017, *The Astronomer's Telegram*, 10747
- Frederick, S., Gezari, S., Graham, M. J., et al. 2019, *ApJ*, 833, 31
- French, K. D., Arcavi, I., & Zabludoff, A. 2016, *ApJL*, 818, L21
- French, K. D., Arcavi, I., Zabludoff, A. I., et al. 2020, *ApJ*, 891, 93
- Fritz, J., Franceschini, A., & Hatziminaoglou, E. 2006, *MNRAS*, 366, 767
- Gal-Yam, A., Mazzali, P. A., Manulis, I., et al. 2013, *PASP*, 125, 749
- Gal-Yam, A. 2019, *ARA&A*, 57, 305
- Gezari, S., Heckman, T., Cenko, S. B., et al. 2009, *ApJ*, 698, 1367
- Gezari, S., Hung, T., Cenko, S. B., et al. 2017, *ApJ*, 835, 144
- Goobar, A., Amanullah, R., Kulkarni, S. R., et al. 2017, *Science*, 356, 491
- Graham, M. J., Djorgovski, S. G., Drake, A. J., et al. 2017, *MNRAS*, 470, 4112
- Graham, M. J., Kulkarni, S. R., Bellm, E. C., et al. 2019, *PASP*, 131, 1001
- Graham, M. J., Ross, N. P., Stern, D., et al. 2019, *MNRAS*, 491, 4925
- Greene, J. E., & Ho, L. C. 2007, *ApJ*, 670, 92
- Greiner, J., Schwarz, R., Zharikov, S., & Orio, M. 2000, *A&A*, 362, L25
- Grupe, D., Thomas, H.-C., & Leighly, K. M. 1999, *A&A*, 350, L31
- Guillochon, J. 2017, *Nature Astronomy*, 1, 0068
- Haehnelt, M. G., & Rees, M. J. 1993, *MNRAS*, 263, 168
- Harris, C. E., Nugent, P. E., Horesh, A., et al. 2018, *ApJ*, 868, 21
- Hills, J. G. 1975, *Nature*, 254, 295
- Hoffman, D. I., Cutri, R. M., Masci, F. J., et al. 2012, *AJ*, 143, 118
- Holoien, T. W.-S., Kochanek, C. S., Prieto, J. L., et al. 2016, *MNRAS*, 455, 2918
- Hutsemékers, D., Agís González, B., Sluse, D., Ramos Almeida, C., & Acosta Pulido, J.-A. 2017, *A&A*, 604, L3
- Hutsemékers, D., Agís González, B., Marin, F., et al. 2019, *A&A*, 625, A54
- Jencson, J. E., Kasliwal, M. M., Adams, S. M., et al. 2019, *ApJ*, 886, 40
- Jiang, N., Zhou, H.-Y., Ho, L. C., et al. 2012, *ApJL*, 759, L31
- Jiang, N., Dou, L., Wang, T., et al. 2016, *ApJL*, 828, L14
- Jiang, N., Wang, T., Yan, L., et al. 2017, *ApJ*, 850, 63
- Jiang, N. 2018, *Research Notes of the American Astronomical Society*, 2, 134
- Jiang, N., Wang, T., Mou, G., et al. 2019, *ApJ*, 871, 15
- Jiang, N., Wang, T., Hu, X., et al. 2021, *ApJ* submitted
- Kaiser, N. 2004, in *Proc. SPIE*, Vol. 5489, *Ground-based Telescopes*, ed. J. M. Oschmann, Jr., 11-22
- Kankare, E., Kotak, R., Mattila, S., et al. 2017, *Nature Astronomy*, 1, 865
- Karas, V., & Šubr, L. 2007, *A&A*, 470, 11
- Kasliwal, M. M., Bally, J., Masci, F., et al. 2017, *ApJ*, 839, 88
- Kaspi, S., Maoz, D., Netzer, H., et al. 2005, *ApJ*, 629, 61
- Kellermann, K. I., Sramek, R., Schmidt, M., et al. 1989, *AJ*, 98, 1195
- Kellermann, K. I., Condon, J. J., Kimball, A. E., Perley, R. A., & Ivezić, Ž. 2016, *ApJ*, 831, 168
- Kewley, L. J., Groves, B., Kauffmann, G., & Heckman, T. 2006, *MNRAS*, 372, 961
- Kochanek, C. S., Shappee, B. J., Stanek, K. Z., et al. 2017, *PASP*, 129, 104502
- Komossa, S. 2015, *Journal of High Energy Astrophysics*, 7, 148
- Kormendy, J., & Ho, L. C. 2013, *ARA&A*, 51, 511
- Koshida, S., Minezaki, T., Yoshii, Y., et al. 2014, *ApJ*, 788, 159
- Kostrzewa-Rutkowska, Z., Jonker, P. G., Hodgkin, S. T., 2018, *MNRAS*, 481, 307
- Kozłowski, S., Kochanek, C. S., Stern, D., et al. 2010, *ApJ*, 722, 1624
- Kozłowski, S., Kochanek, C. S., Ashby, Matthew L. N., et al. 2010, *ApJ*, 722, 1624
- Kroupa, P. 2001, *MNRAS*, 322, 231
- LaMassa, S. M., Cales, S., Moran, E. C., et al. 2015, *ApJ*, 800, 144
- Lamastra, A., Bianchi, S., Matt, G., et al. 2009, *A&A*, 504, 73
- Laor, A., & Draine, B. T. 1993, *ApJ*, 402, 441
- Lazo, B., Zahid, H. J., Sohn, J., et al. 2018, *Research Notes of the American Astronomical Society*, 2, 234
- Law, N. M., Kulkarni, S. R., Dekany, R. G., et al. 2009, *PASP*, 121, 1395
- Law-Smith, J., Ramirez-Ruiz, E., Ellison, S. L., & Foley, R. J. 2017, *ApJ*, 850, 22
- Lawrence, A.; Warren, S. J.; Almaini, O. 2007, *MNRAS*, 379, 1599
- Leloudas, G., Fraser, M., Stone, N. C., et al. 2016, *Nature Astronomy*, 1, 0002
- Lezhnin, K., & Vasiliev, E. 2015, *ApJL*, 808, L5
- Liao, N.-H., Dou, L.-M., Jiang, N., et al. 2019, *ApJL*, 879, L9
- Liu, H.-Y., Liu, W.-J., Dong, X.-B., et al. 2019, *ApJS*, 243, 21
- Lu, H., Zhou, H., Wang, J., et al. 2006, *AJ*, 131, 790
- Lu, W., Kumar, P., & Evans, N. J. 2016, *MNRAS*, 458, 575
- Lu, W., Kumar, P., & Narayan, R. 2017, *MNRAS*, 468, 910
- Lu, W., & Kumar, P. 2018, *ApJ*, 865, 128
- Lyu, J., Rieke, G. H., & Smith, P. S. 2019, *ApJ*, 886, 33
- MacLeod, C. L., Ross, N. P., Lawrence, A., et al. 2016, *MNRAS*, 457, 389
- Mathis, J. S., Rimpl, W., & Nordsieck, K. H. 1977, *ApJ*, 217, 425
- McConnell, N. J., & Ma, C.-P. 2013, *ApJ*, 764, 184
- McElroy, R. E., Husemann, B., Croom, S. M., et al. 2016, *A&A*, 593, L8
- Mainzer, A., Bauer, J., Grav, T., et al. 2011, *ApJ*, 731, 53
- Mainzer, A., Bauer, J., Cutri, R. M., et al. 2014, *ApJ*, 792, 30
- Maraston, C., Pforr, J., Henriques, B. M., et al. 2013, *MNRAS*, 435, 2764
- Martin, D. C., Fanson, J., Schiminovich, D., et al. 2005, *ApJL*, 619, L1
- Mattila, S., Pérez-Torres, M., Efstathiou, A., et al. 2018, *Science*, 361, 482
- Meisner, A. M., Lang, D., & Schlegel, D. J. 2018, *AJ*, 156, 69
- Mockler, B., Guillochon, J., & Ramirez-Ruiz, E. 2019, *ApJ*, 872, 151
- Mor, R., & Netzer, H. 2012, *MNRAS*, 420, 526
- Moustakas, J., Coil, A. L., Aird, J., et al. 2013, *ApJ*, 767, 50
- Namekata, D., & Umemura, M. 2016, *MNRAS*, 460, 980
- Neukova, M.; Sirocky, M. M.; Ivezić, Z.; Elitzur, M. 2008, *ApJ*, 685, 147
- Oknyansky, V. L., Winkler, H., Tsygankov, S. S., et al. 2019, *MNRAS*, 483, 558
- Pasham, D. R., Remillard, R. A., Fragile, P. C., et al. 2019, *Science*, 363, 531
- Phinney, E. S. 1989, *The Center of the Galaxy*, 136, 543
- Rees, M. J. 1988, *Nature*, 333, 523
- Reines, A. E., & Volonteri, M. 2015, *ApJ*, 813, 82
- Ross, N., Assef, R. J., Kirkpatrick, J. D., Graham, M. J. 2019, *BAAS*, 51, 321
- Roth, N., Rossi, E. M., Krolik, J. H., et al. 2020, *arXiv:2008.01117*
- Runnoe, J. C., Brotherton, M. S., & Shang, Z. 2012, *MNRAS*, 422, 478
- Runnoe, J. C., Cales, S., Ruan, J. J., et al. 2016, *MNRAS*, 455, 1691
- Sabater, J., Best, P. N., Harcastle, M. J., et al. 2019, *A&A*, 622, A17
- Sarzi, M., Falcón-Barroso, J., Davies, R. L., et al. 2006, *MNRAS*, 366, 1151
- Schlegel, D. J., Finkbeiner, D. P., & Davis, M. 1998, *ApJ*, 500, 525
- Schechter, P. 1976, *ApJ*, 203, 297
- Schmidt, M. 1968, *ApJ*, 151, 393
- Shappee, B. J., Prieto, J. L., Grupe, D., et al. 2014, *ApJ*, 788, 48
- Sheng, Z., Wang, T., Jiang, N., et al. 2017, *ApJL*, 846, L7
- Sheng, Z., Wang, T., Jiang, N., et al. 2020, *ApJ*, 889, 46
- Skrutskie, M. F., Cutri, R. M., Stiening, R., et al. 2006, *AJ*, 131, 1163
- Stalewski, M.; Fritz, J.; Baes, M.; Nakos, T.; Popović, L.Č. 2012, *MNRAS*, 420, 2756
- Stern, D., McKernan, B., Graham, M. J., et al. 2018, *ApJ*, 864, 27
- Stone, N. C., & Metzger, B. D. 2016, *MNRAS*, 455, 859
- Stone, N. C., Vasiliev, E., Kesden, M., et al. 2020, *SSRv*, 216, 35
- Strauss, M. A., Weinberg, D. H., Lupton, R. H., et al. 2002, *AJ*, 124, 1810
- Strateva, I., Ivezić, Ž., Knapp, G. R., et al. 2001, *AJ*, 122, 1861
- Suganuma, M.; Yoshii, Y.; Kobayashi, Y., et al. 2006, *ApJ*, 639, 46
- Sun, L., Jiang, N., Wang, T., et al. 2020, *ApJ*, 898, 129
- Svirski, G., Piran, T., & Krolik, J. 2017, *MNRAS*, 467, 1426
- Tadhunter, C., Spence, R., Rose, M., Mullaney, J., & Crowther, P. 2017, *Nature Astronomy*, 1, 0061
- Thomas, D., Steele, O., Maraston, C., et al. 2013, *MNRAS*, 431, 1383
- Tinyanont, S., Kasliwal, M. M., Fox, O. D., et al. 2016, *ApJ*, 833, 231
- Tonry, J. L., Denneau, L., Heinze, A. N., et al. 2018, *PASP*, 130, 988
- Trakhtenbrot, B., Arcavi, I., Ricci, C., et al. 2019, *Nature Astronomy*, 3, 242
- Ulrich, M.-H., Maraschi, L., & Urry, C. M. 1997, *ARA&A*, 35, 445
- van der Marel, R. P., Alves, D. R., Hardy, E., & Suntzeff, N. B. 2002, *AJ*, 124, 2639
- van Velzen, S., & Farrar, G. R. 2014, *ApJ*, 792, 53
- van Velzen, S., Mendez, A. J., Krolik, J. H., & Gorjian, V. 2016, *ApJ*, 829, 19
- van Velzen, S. 2018, *ApJ*, 852, 72
- van Velzen, S., Gezari, S., Hammerstein, E., et al. 2020, *arXiv e-prints*, *arXiv:2001.01409*
- Wang, J., & Merritt, D. 2004, *ApJ*, 600, 149
- Wang, T.-G., Zhou, H.-Y., Komossa, S., et al. 2012, *ApJ*, 749, 115
- Wang, T., Yan, L., Dou, L., et al. 2018, *MNRAS*, 477, 2583
- Wang, T.-gui., Jiang, N., Ge, J., et al. 2019, *ApJL*, 886, L5
- Wevers, T., Pasham, D. R., van Velzen, S., et al. 2019, *MNRAS*, 488, 4816
- Wright, E. L., Eisenhardt, P. R. M., Mainzer, A. K., et al. 2010, *AJ*, 140, 1868-1881
- Xiao, T., Barth, A. J., Greene, J. E., et al. 2011, *ApJ*, 739, 28
- Yan, L., Donoso, E., Tsai, C.-W., et al. 2013, *AJ*, 145, 55
- Yan, L., Wang, T., Jiang, N., et al. 2019, *ApJ*, 874, 44
- Yang, C.-W., Wang, T.-G., Ferland, G., et al. 2013, *ApJ*, 774, 46
- Yang, Q., Wu, X.-B., Fan, X., et al. 2018, *ApJ*, 862, 109
- Zahid, H. J., Geller, M. J., Fabricant, D. G., et al. 2016, *ApJ*, 832, 203

Table 1. The properties of MIR flares

Name	RA	DEC	$z$	$\Delta W1$	$\Delta W2$	W1m	W2m	$L_{W1}$	$L_{W2}$	$\Delta d$
(1)	(2)	(3)	(4)	mag	mag	mag	mag	erg s <sup>-1</sup>	erg s <sup>-1</sup>	arcsec
(1)	(2)	(3)	(4)	(5)	(6)	(7)	(8)	(9)	(10)	(11)
SDSSJ000046.46+143813.0	0.193583	14.6369	0.13660	0.32±0.05	0.58±0.05	-24.19±0.14	-25.37±0.08	43.19±0.06	43.27±0.03	0.08
SDSSJ002701.03+071357.6	6.754291	7.23266	0.13109	0.37±0.03	0.60±0.06	-23.91±0.07	-24.94±0.10	43.08±0.03	43.10±0.04	0.02
SDSSJ004500.47-004723.1	11.25195	-0.7897	0.05677	0.72±0.04	1.17±0.16	-21.99±0.06	-22.93±0.10	42.31±0.02	42.30±0.04	0.43
SDSSJ010320.42+140149.8	15.83508	14.0305	0.04181	1.29±0.03	1.90±0.02	-25.34±0.01	-26.30±0.01	43.65±0.01	43.64±0.00	0.07
SDSSJ012047.99-082918.4	20.19995	-8.4884	0.03468	0.42±0.03	0.55±0.02	-24.10±0.07	-25.02±0.04	43.16±0.03	43.13±0.02	0.07
SDSSJ012100.67+140517.3	20.25279	14.0881	0.12938	0.36±0.03	0.61±0.07	-23.35±0.12	-24.88±0.14	42.85±0.05	43.08±0.06	0.11
SDSSJ015804.75-005221.8	29.51979	-0.8727	0.08044	2.16±0.04	2.71±0.11	-24.60±0.02	-25.56±0.03	43.35±0.01	43.35±0.01	0.09
SDSSJ020552.16+000411.8	31.46733	0.06994	0.07649	1.17±0.01	1.76±0.09	-24.81±0.02	-25.85±0.03	43.44±0.01	43.46±0.01	0.09
SDSSJ074547.87+265537.9	116.4494	26.9271	0.11481	0.73±0.07	0.82±0.04	-24.81±0.08	-25.99±0.04	43.44±0.03	43.52±0.02	0.11
SDSSJ075709.69+190842.8	119.2903	19.1452	0.10501	0.38±0.02	0.69±0.07	-23.78±0.05	-24.83±0.08	43.02±0.02	43.05±0.03	0.07
SDSSJ081121.40+405451.8	122.8391	40.9143	0.06704	0.63±0.02	0.52±0.03	-24.88±0.03	-25.75±0.06	43.47±0.01	43.42±0.02	0.04
SDSSJ081403.78+261144.3	123.5157	26.1956	0.07567	0.26±0.03	0.61±0.01	-23.23±0.15	-24.77±0.03	42.81±0.06	43.03±0.01	0.09
SDSSJ081451.87+533732.5	123.7161	53.6256	0.13901	0.47±0.01	0.83±0.06	-24.16±0.03	-25.27±0.06	43.18±0.01	43.23±0.02	0.09
SDSSJ083536.49+493542.7	128.9020	49.5951	0.04238	0.75±0.08	1.38±0.02	-23.55±0.08	-24.66±0.01	42.93±0.03	42.99±0.00	0.10
SDSSJ083721.86+414342.0	129.3410	41.7283	0.09806	0.31±0.02	0.58±0.08	-24.06±0.07	-25.22±0.12	43.14±0.03	43.21±0.05	0.09
SDSSJ084157.98+052605.7	130.4915	5.43491	0.15631	0.44±0.03	0.65±0.04	-24.95±0.07	-25.95±0.06	43.49±0.03	43.50±0.02	0.15
SDSSJ084232.87+235719.6	130.6369	23.9554	0.06353	0.51±0.04	0.76±0.02	-23.06±0.09	-23.80±0.04	42.74±0.03	42.64±0.02	0.06
SDSSJ084752.78+514236.2	131.9699	51.7100	0.11997	0.23±0.08	0.61±0.04	-22.86±0.33	-24.37±0.08	42.66±0.13	42.87±0.03	0.08
SDSSJ085434.65+111334.7	133.6443	11.2263	0.16719	0.42±0.03	0.56±0.03	-25.77±0.06	-26.66±0.05	43.82±0.02	43.79±0.02	0.08
SDSSJ085835.90+412113.8	134.6495	41.3538	0.08705	0.19±0.06	0.53±0.07	-21.12±0.60	-23.14±0.17	41.96±0.24	42.38±0.07	0.10
SDSSJ085959.46+092225.6	134.9977	9.37377	0.15188	1.09±0.03	1.49±0.08	-25.56±0.03	-26.59±0.03	43.74±0.01	43.76±0.01	0.01
SDSSJ090924.55+192004.8	137.3522	19.3346	0.10716	0.62±0.06	1.29±0.08	-23.64±0.10	-25.13±0.05	42.97±0.04	43.17±0.02	0.15
SDSSJ091531.04+481407.7	138.8793	48.2354	0.10049	0.54±0.02	0.75±0.05	-24.29±0.03	-25.08±0.06	43.23±0.01	43.16±0.02	0.05
SDSSJ093135.46+662652.2	142.8977	66.4478	0.08729	0.27±0.02	0.52±0.04	-22.78±0.07	-23.73±0.09	42.63±0.03	42.62±0.03	0.07
SDSSJ093608.58+061525.4	144.0357	6.25705	0.00800	0.70±0.03	0.79±0.06	-18.29±0.04	-18.52±0.09	40.83±0.02	40.53±0.04	1.49
SDSSJ094303.26+595809.3	145.7635	59.9692	0.07491	0.25±0.01	0.67±0.04	-21.62±0.06	-23.07±0.07	42.16±0.03	42.35±0.03	0.20
SDSSJ094456.56+310552.2	146.2356	31.0978	0.03465	0.42±0.04	0.84±0.04	-22.99±0.10	-23.95±0.03	42.71±0.04	42.70±0.01	0.12
SDSSJ095754.76+020711.2	149.4781	2.11977	0.12528	0.40±0.05	0.60±0.07	-24.01±0.11	-24.98±0.11	43.12±0.04	43.11±0.04	0.01
SDSSJ100120.37+182926.6	150.3348	18.4907	0.10603	0.37±0.06	0.74±0.12	-22.99±0.14	-24.13±0.18	42.71±0.06	42.78±0.07	0.30
SDSSJ100256.90+442457.8	150.7370	44.4160	0.15446	0.16±0.02	0.62±0.05	-23.62±0.12	-25.54±0.07	42.96±0.05	43.34±0.03	0.18
SDSSJ100350.97+020227.6	150.9623	2.04100	0.12470	0.63±0.02	0.90±0.09	-24.29±0.03	-25.13±0.08	43.23±0.01	43.17±0.03	0.01
SDSSJ100809.02+154951.3	152.0375	15.8309	0.11765	0.55±0.02	0.81±0.10	-24.60±0.04	-25.63±0.10	43.35±0.01	43.37±0.04	0.15
SDSSJ100931.70+343604.7	152.3820	34.6013	0.20863	0.45±0.04	0.69±0.08	-24.94±0.08	-26.03±0.10	43.49±0.03	43.53±0.04	0.08
SDSSJ100955.70+220949.3	152.4820	22.1636	0.14153	0.49±0.03	0.66±0.06	-24.90±0.05	-25.80±0.08	43.48±0.02	43.44±0.03	0.03
SDSSJ101157.62+534857.9	152.9900	53.8160	0.23440	0.47±0.05	0.70±0.07	-25.62±0.11	-26.78±0.08	43.76±0.04	43.83±0.03	0.05
SDSSJ101708.94+122412.0	154.2872	12.4033	0.10762	0.61±0.04	0.95±0.05	-23.66±0.06	-24.60±0.06	42.98±0.02	42.96±0.02	0.05
SDSSJ102017.72+251554.3	155.0738	25.2650	0.13145	0.54±0.04	1.06±0.09	-23.50±0.09	-24.67±0.08	42.91±0.04	42.99±0.03	0.18
SDSSJ102934.88+252635.8	157.3953	25.4432	0.23761	0.91±0.02	0.85±0.08	-26.11±0.03	-26.64±0.08	43.96±0.01	43.78±0.03	0.14
SDSSJ102959.95+482937.9	157.4997	48.4938	0.23235	0.78±0.10	0.89±0.03	-25.95±0.10	-26.91±0.04	43.89±0.04	43.89±0.01	0.02
SDSSJ103753.68+391249.6	159.4736	39.2137	0.10677	0.46±0.03	1.07±0.08	-23.31±0.08	-24.78±0.07	42.84±0.03	43.03±0.03	0.06
SDSSJ104138.79+341253.5	160.4116	34.2148	0.14028	0.42±0.04	0.62±0.12	-24.30±0.11	-25.14±0.16	43.23±0.04	43.18±0.06	0.07
SDSSJ104306.56+271602.1	160.7773	27.2672	0.12812	0.90±0.06	1.46±0.05	-24.45±0.06	-25.42±0.04	43.29±0.02	43.29±0.02	0.27
SDSSJ104609.61+165511.4	161.5400	16.9198	0.20687	0.42±0.04	0.54±0.05	-25.59±0.09	-26.60±0.09	43.75±0.04	43.76±0.03	0.07
SDSSJ105145.47+210132.1	162.9394	21.0255	0.06593	0.35±0.03	0.60±0.07	-22.24±0.09	-23.24±0.11	42.41±0.04	42.42±0.04	0.10
SDSSJ105344.12+552405.7	163.4338	55.4015	0.15174	0.27±0.03	0.51±0.04	-23.84±0.14	-25.14±0.09	43.05±0.06	43.18±0.03	0.07
SDSSJ105801.52+544437.0	164.5063	54.7436	0.13062	0.30±0.03	0.77±0.04	-23.43±0.10	-24.98±0.05	42.89±0.04	43.11±0.02	0.06
SDSSJ110501.98+594103.5	166.2582	59.6843	0.03369	0.94±0.02	1.26±0.02	-24.22±0.02	-24.96±0.01	43.20±0.01	43.11±0.01	0.08
SDSSJ110958.34+370809.6	167.4930	37.1360	0.02602	0.44±0.02	0.93±0.03	-22.63±0.05	-23.69±0.03	42.57±0.02	42.60±0.01	0.14
SDSSJ111122.44+592334.3	167.8435	59.3928	0.16973	0.47±0.02	0.71±0.07	-24.48±0.05	-25.34±0.09	43.31±0.02	43.26±0.03	0.06

Table 1 continued

Table 1 (continued)

Name	RA	DEC	$z$	$\Delta W1$	$\Delta W2$	W1m	W2m	$L_{W1}$	$L_{W2}$	$\Delta d$
(1)	(2)	(3)	(4)	mag	mag	mag	mag	erg s <sup>-1</sup>	erg s <sup>-1</sup>	arcsec
(1)	(2)	(3)	(4)	(5)	(6)	(7)	(8)	(9)	(10)	(11)
SDSSJ11431.83+405613.8	168.6326	40.9371	0.15247	0.50±0.03	0.57±0.02	-25.20±0.07	-26.11±0.03	43.60±0.03	43.57±0.01	0.07
SDSSJ11536.57+054449.7	168.9023	5.74713	0.08995	1.08±0.12	1.85±0.28	-24.39±0.08	-25.58±0.06	43.27±0.03	43.35±0.03	0.33
SDSSJ112018.31+193345.8	170.0762	19.5627	0.12780	0.76±0.05	0.94±0.07	-25.22±0.05	-26.03±0.06	43.60±0.02	43.54±0.02	0.16
SDSSJ112238.84+143348.4	170.6618	14.5634	0.19421	0.51±0.02	0.52±0.02	-25.76±0.04	-26.53±0.05	43.82±0.02	43.73±0.02	0.05
SDSSJ112446.21+045525.4	171.1925	4.92372	0.07398	0.36±0.02	0.83±0.04	-23.37±0.06	-24.89±0.04	42.86±0.02	43.08±0.02	0.09
SDSSJ112916.12+513123.5	172.3171	51.5231	0.03286	0.21±0.02	0.74±0.02	-22.24±0.09	-24.06±0.02	42.41±0.04	42.75±0.01	0.04
SDSSJ113355.93+670107.0	173.4830	67.0186	0.03968	0.50±0.04	0.71±0.08	-23.37±0.09	-24.29±0.09	42.86±0.04	42.84±0.04	0.02
SDSSJ113901.27+613408.5	174.7552	61.5690	0.13461	0.30±0.01	0.65±0.05	-23.68±0.06	-25.17±0.06	42.99±0.02	43.19±0.03	0.08
SDSSJ114922.02+544151.4	177.3417	54.6976	0.06190	0.77±0.01	1.14±0.10	-23.53±0.02	-24.38±0.06	42.93±0.01	42.88±0.02	0.17
SDSSJ115205.33+485049.9	178.0222	48.8471	0.15102	0.85±0.07	1.06±0.06	-25.42±0.06	-26.33±0.04	43.68±0.02	43.65±0.02	0.08
SDSSJ115326.76+403719.1	178.3615	40.6219	0.14510	0.62±0.04	0.96±0.04	-24.51±0.07	-25.56±0.03	43.32±0.03	43.35±0.01	0.20
SDSSJ120057.93+064823.1	180.2413	6.80641	0.03599	0.45±0.04	0.80±0.05	-24.10±0.08	-25.47±0.05	43.15±0.03	43.31±0.02	0.05
SDSSJ120145.97+352522.5	180.4415	35.4229	0.19031	0.64±0.03	0.95±0.03	-25.52±0.05	-26.64±0.03	43.72±0.02	43.78±0.01	0.04
SDSSJ120338.31+585911.8	180.9096	58.9866	0.04692	0.54±0.04	1.03±0.06	-21.37±0.08	-22.59±0.06	42.06±0.03	42.16±0.02	0.09
SDSSJ120842.69+330523.0	182.1778	33.0897	0.28028	0.38±0.08	0.54±0.07	-25.09±0.21	-26.17±0.18	43.55±0.08	43.59±0.07	0.18
SDSSJ120942.22+320258.8	182.4259	32.0496	0.05898	0.70±0.02	1.01±0.02	-24.34±0.03	-25.22±0.02	43.25±0.01	43.21±0.01	0.13
SDSSJ121130.30+404743.2	182.8762	40.7953	0.34779	0.75±0.03	0.88±0.11	-26.45±0.04	-27.42±0.10	44.10±0.02	44.09±0.04	0.17
SDSSJ121457.41+101418.1	183.7392	10.2383	0.14583	0.91±0.03	1.40±0.21	-24.77±0.03	-25.79±0.10	43.42±0.01	43.44±0.04	0.24
SDSSJ121825.51+295154.8	184.6062	29.8652	0.13559	0.85±0.04	1.39±0.08	-24.73±0.05	-25.95±0.05	43.41±0.02	43.50±0.02	0.02
SDSSJ121907.89+051645.6	184.7828	5.27933	0.08251	1.12±0.04	1.64±0.07	-24.03±0.03	-25.05±0.03	43.13±0.01	43.14±0.01	0.04
SDSSJ122823.86+361729.0	187.0994	36.2913	0.13369	0.86±0.02	1.28±0.10	-24.58±0.03	-25.50±0.05	43.35±0.01	43.32±0.02	0.09
SDSSJ123852.87+081512.0	189.7202	8.25333	0.11378	0.68±0.03	1.04±0.02	-24.40±0.03	-25.48±0.03	43.28±0.01	43.31±0.01	0.15
SDSSJ124255.36+253727.9	190.7306	25.6244	0.08789	0.58±0.03	1.15±0.09	-23.00±0.05	-24.12±0.07	42.72±0.02	42.77±0.03	0.05
SDSSJ124521.42-014735.4	191.3392	-1.7931	0.21543	0.37±0.05	0.78±0.08	-24.56±0.17	-26.06±0.10	43.34±0.07	43.55±0.04	0.05
SDSSJ130355.93+220338.7	195.9830	22.0607	0.09601	0.38±0.04	0.52±0.07	-23.80±0.10	-24.52±0.12	43.03±0.04	42.93±0.05	0.13
SDSSJ130532.91+395337.9	196.3871	39.8938	0.07249	0.67±0.02	1.08±0.04	-23.78±0.03	-24.67±0.03	43.03±0.01	42.99±0.01	0.05
SDSSJ130815.57+042909.6	197.0648	4.48600	0.04832	0.35±0.03	0.71±0.05	-22.81±0.08	-23.76±0.06	42.64±0.03	42.63±0.02	0.01
SDSSJ131022.77+251809.2	197.5948	25.3025	0.16039	0.55±0.04	0.64±0.08	-24.59±0.08	-25.57±0.11	43.35±0.03	43.35±0.04	0.03
SDSSJ131509.34+072737.6	198.7889	7.46044	0.09182	0.66±0.02	0.95±0.04	-24.77±0.03	-25.56±0.03	43.42±0.01	43.35±0.01	0.05
SDSSJ132259.94+330121.9	200.7497	33.0227	0.12690	0.35±0.02	0.65±0.03	-24.20±0.06	-25.35±0.05	43.19±0.02	43.26±0.02	0.08
SDSSJ132848.45+275227.8	202.2018	27.8743	0.09114	0.60±0.05	0.81±0.07	-24.22±0.06	-25.16±0.07	43.20±0.03	43.19±0.03	0.04
SDSSJ132902.05+234108.4	202.2585	23.6856	0.07171	0.55±0.03	1.32±0.04	-23.08±0.06	-24.60±0.03	42.75±0.02	42.96±0.01	0.13
SDSSJ133212.62+203637.9	203.0525	20.6105	0.11249	1.16±0.01	1.58±0.03	-25.48±0.02	-26.48±0.02	43.71±0.01	43.71±0.01	0.22
SDSSJ133731.36+003528.8	204.3806	0.59133	0.29881	0.72±0.09	0.74±0.05	-27.36±0.09	-28.23±0.05	44.46±0.04	44.42±0.02	0.12
SDSSJ134032.49+184218.6	205.1353	18.7051	0.09018	0.37±0.06	0.65±0.07	-22.76±0.14	-23.81±0.10	42.62±0.06	42.64±0.04	0.08
SDSSJ134105.98-004902.4	205.2749	-0.8173	0.17538	0.61±0.05	0.66±0.08	-25.43±0.08	-26.25±0.10	43.69±0.03	43.62±0.04	0.09
SDSSJ134123.20+151650.4	205.3466	15.2806	0.12553	0.39±0.03	0.72±0.04	-23.87±0.10	-25.16±0.05	43.06±0.04	43.19±0.02	0.12
SDSSJ134849.38+155902.0	207.2057	15.9838	0.18237	0.83±0.05	1.11±0.05	-25.83±0.07	-26.85±0.06	43.85±0.03	43.86±0.02	0.11
SDSSJ135241.36+000925.8	208.1723	0.15716	0.16596	0.37±0.04	0.60±0.04	-24.25±0.12	-25.40±0.07	43.22±0.05	43.28±0.03	0.20
SDSSJ140221.26+392212.3	210.5885	39.3700	0.06375	1.65±0.01	2.15±0.04	-24.97±0.01	-25.73±0.01	43.50±0.00	43.42±0.00	0.22
SDSSJ140648.43+062834.8	211.7017	6.47633	0.08499	0.35±0.01	0.70±0.03	-24.10±0.04	-25.28±0.04	43.16±0.02	43.23±0.01	0.13
SDSSJ140950.27+105740.2	212.4594	10.9611	0.05972	0.19±0.02	0.54±0.05	-23.06±0.14	-24.65±0.08	42.74±0.06	42.98±0.03	0.15
SDSSJ141235.89+411458.5	213.1495	41.2495	0.10250	0.34±0.02	0.54±0.03	-23.73±0.06	-24.48±0.07	43.00±0.02	42.91±0.03	0.08
SDSSJ142254.11+060953.4	215.7254	6.16483	0.05636	0.77±0.02	1.23±0.02	-24.85±0.03	-25.67±0.01	43.45±0.01	43.39±0.00	0.19
SDSSJ142420.78+624916.5	216.0865	62.8212	0.10913	0.41±0.04	0.59±0.02	-24.27±0.09	-25.06±0.03	43.22±0.03	43.15±0.01	0.05
SDSSJ142808.89-023124.8	217.0370	-2.5235	0.05207	0.37±0.07	0.50±0.13	-21.67±0.18	-22.68±0.30	42.18±0.07	42.19±0.12	0.03
SDSSJ143016.05+230344.4	217.5668	23.0623	0.08105	0.56±0.01	0.74±0.05	-24.94±0.03	-25.69±0.06	43.49±0.01	43.40±0.02	0.02
SDSSJ144024.32+175852.7	220.1013	17.9813	0.11574	0.43±0.04	0.54±0.07	-22.73±0.15	-23.84±0.13	42.61±0.06	42.66±0.05	0.03
SDSSJ144227.57+555846.3	220.6148	55.9795	0.07689	1.39±0.02	1.79±0.03	-26.07±0.01	-26.86±0.01	43.94±0.00	43.86±0.00	0.04
SDSSJ144758.41+402335.8	221.9933	40.3932	0.13025	0.89±0.02	1.22±0.04	-25.40±0.02	-26.20±0.02	43.67±0.01	43.60±0.01	0.05
SDSSJ144829.01+113732.1	222.1208	11.6255	0.06657	0.58±0.03	1.15±0.02	-23.14±0.05	-24.35±0.02	42.77±0.02	42.86±0.01	0.23
SDSSJ150440.39+010735.0	226.1682	1.12638	0.12826	0.61±0.03	0.61±0.03	-26.39±0.04	-27.24±0.04	44.07±0.02	44.02±0.02	0.11

Table 1 continued

Table 1 (continued)

Name	RA	DEC	$z$	$\Delta W1$	$\Delta W2$	W1m	W2m	$L_{W1}$	$L_{W2}$	$\Delta d$
(1)	(2)	(3)	(4)	mag	mag	mag	mag	erg s <sup>-1</sup>	erg s <sup>-1</sup>	arcsec
SDSSJ150844.22+260249.1	227.1842	26.0469	0.08255	0.28±0.03	0.73±0.06	-22.47±0.13	-24.12±0.07	42.50±0.05	42.77±0.03	0.11
SDSSJ151117.94+221428.2	227.8247	22.2411	0.12048	0.37±0.04	0.64±0.05	-24.11±0.10	-25.36±0.07	43.16±0.04	43.27±0.03	0.08
SDSSJ151257.18+280937.5	228.2382	28.1604	0.11552	0.28±0.03	0.67±0.04	-23.19±0.12	-24.61±0.06	42.79±0.05	42.97±0.02	0.01
SDSSJ151345.76+311125.0	228.4406	31.1902	0.07181	0.81±0.01	1.16±0.03	-24.21±0.02	-25.01±0.02	43.20±0.01	43.13±0.01	0.01
SDSSJ152438.13+531458.7	231.1588	53.2496	0.08513	0.67±0.05	0.85±0.05	-23.21±0.06	-23.97±0.05	42.80±0.02	42.71±0.02	0.10
SDSSJ153151.41+372445.9	232.9642	37.4127	0.02990	1.43±0.04	1.84±0.10	-21.37±0.03	-22.24±0.03	42.06±0.01	42.02±0.01	0.99
SDSSJ153310.02+272920.2	233.2917	27.4889	0.07193	0.53±0.07	0.69±0.09	-24.52±0.13	-25.53±0.10	43.32±0.05	43.33±0.04	0.03
SDSSJ153711.29+581420.2	234.2970	58.2389	0.09356	1.28±0.08	1.47±0.11	-25.18±0.04	-26.04±0.04	43.59±0.01	43.54±0.02	0.06
SDSSJ154029.29+005437.2	235.1220	0.91033	0.01172	0.37±0.06	0.62±0.11	-17.76±0.16	-18.79±0.17	40.62±0.06	40.64±0.07	0.63
SDSSJ154158.63+071836.4	235.4942	7.31011	0.16305	0.42±0.05	0.79±0.11	-23.92±0.11	-25.08±0.12	43.08±0.04	43.16±0.05	0.06
SDSSJ154843.06+220812.6	237.1794	22.1368	0.03127	2.12±0.02	2.90±0.04	-24.00±0.01	-24.91±0.01	43.12±0.00	43.09±0.00	0.01
SDSSJ154955.19+332752.0	237.4799	33.4644	0.08565	1.44±0.04	2.09±0.05	-24.29±0.02	-25.20±0.02	43.23±0.01	43.20±0.01	0.03
SDSSJ155437.26+525526.4	238.6552	52.9240	0.06644	0.71±0.01	1.32±0.01	-23.62±0.01	-24.76±0.01	42.96±0.00	43.03±0.00	0.11
SDSSJ155438.39+163637.6	238.6599	16.6104	0.00798	0.60±0.05	1.03±0.12	-17.63±0.07	-18.47±0.08	40.56±0.03	40.51±0.03	0.83
SDSSJ155440.25+362952.0	238.6677	36.4977	0.23683	0.76±0.04	1.01±0.16	-25.91±0.04	-26.80±0.11	43.88±0.02	43.84±0.04	0.11
SDSSJ155539.95+212005.7	238.9164	21.3349	0.07094	0.51±0.02	1.05±0.04	-23.39±0.05	-24.79±0.03	42.87±0.02	43.04±0.01	0.08
SDSSJ155640.32+451338.4	239.1680	45.2273	0.18083	0.64±0.07	0.86±0.08	-24.88±0.09	-25.95±0.07	43.47±0.04	43.50±0.03	0.04
SDSSJ155743.52+272753.0	239.4313	27.4647	0.03156	0.28±0.01	0.79±0.01	-22.62±0.05	-24.30±0.02	42.56±0.02	42.84±0.01	0.03
SDSSJ160052.26+461242.9	240.2177	46.2119	0.19742	0.32±0.02	0.62±0.04	-24.72±0.07	-25.93±0.06	43.40±0.03	43.49±0.03	0.05
SDSSJ161258.17+141617.5	243.2423	14.2715	0.07200	0.29±0.02	0.57±0.03	-22.10±0.08	-23.58±0.06	42.35±0.03	42.56±0.03	0.09
SDSSJ162034.99+240726.5	245.1457	24.1240	0.06551	1.31±0.04	1.64±0.05	-24.17±0.02	-24.80±0.02	43.18±0.01	43.04±0.01	0.14
SDSSJ162810.03+481047.7	247.0417	48.1799	0.12454	0.25±0.03	0.58±0.05	-22.93±0.12	-24.34±0.09	42.69±0.05	42.86±0.03	0.12
SDSSJ163246.84+441618.5	248.1951	44.2718	0.05789	0.49±0.01	0.91±0.02	-23.06±0.03	-23.99±0.02	42.74±0.01	42.72±0.01	0.01
SDSSJ164754.38+384342.0	251.9765	38.7283	0.08547	1.14±0.02	1.68±0.06	-23.99±0.02	-24.91±0.02	43.11±0.01	43.09±0.01	0.05
SDSSJ165726.81+234528.1	254.3617	23.7578	0.05914	2.96±0.03	3.59±0.05	-25.52±0.01	-26.69±0.01	43.72±0.00	43.80±0.00	0.05
SDSSJ165922.65+204947.4	254.8443	20.8298	0.04513	0.17±0.02	0.60±0.02	-22.78±0.11	-24.44±0.04	42.63±0.04	42.90±0.01	0.05
SDSSJ211529.89-001107.0	318.8745	-0.1852	0.23285	0.55±0.06	0.77±0.07	-25.07±0.11	-25.96±0.09	43.54±0.04	43.51±0.03	0.06
SDSSJ214142.90-085702.3	325.4287	-8.9506	0.08729	0.45±0.04	0.76±0.05	-23.29±0.09	-24.38±0.06	42.83±0.04	42.88±0.02	0.12
SDSSJ214603.88+104128.6	326.5161	10.6912	0.16358	0.60±0.05	0.82±0.08	-24.61±0.07	-25.46±0.08	43.36±0.03	43.31±0.03	0.11
SDSSJ215055.73-010654.1	327.7322	-1.1150	0.08791	1.87±0.12	1.90±0.11	-24.29±0.05	-25.00±0.03	43.23±0.02	43.12±0.01	0.03
SDSSJ215648.45+004110.6	329.2018	0.68627	0.05389	0.20±0.02	0.51±0.02	-22.14±0.12	-23.64±0.05	42.37±0.05	42.58±0.02	0.11
SDSSJ220349.23+112433.0	330.9551	11.4091	0.18627	0.95±0.02	1.52±0.09	-25.58±0.03	-26.63±0.04	43.75±0.01	43.78±0.02	0.08
SDSSJ221541.60-010721.0	333.9233	-1.1225	0.04775	0.27±0.03	0.65±0.05	-22.59±0.10	-23.82±0.08	42.55±0.04	42.65±0.03	0.26
SDSSJ231055.38+222008.5	347.7307	22.3356	0.07829	0.25±0.02	0.50±0.05	-22.97±0.06	-24.10±0.09	42.70±0.03	42.76±0.03	0.02
SDSSJ231222.78+133538.8	348.0949	13.5941	0.16553	0.36±0.05	0.60±0.05	-24.09±0.14	-25.17±0.09	43.15±0.06	43.19±0.04	0.02
SDSSJ232452.26+154251.0	351.2177	15.7141	0.15109	0.75±0.02	0.88±0.06	-25.15±0.03	-25.97±0.08	43.58±0.01	43.51±0.03	0.04

NOTE— (1): SDSS name. (2)-(4): RA, DEC and redshift given by SDSS. (5)-(6): The amplitudes of variability in W1 and W2 bands. (7)-(8): The peak absolute magnitude in W1 and W2. (9)-(10): The peak monochromatic luminosity of W1 and W2. (11): The offset distance between the maximum outburst epoch and quiescent state.

Table 2. The fitted dust parameters

Name	$T_{bb}$	$\log L_{bb}$	$\log M_{bb}$	$\log R_{bb}$	$T_d$	$\log L_d$	$\log M_d$	$\log R_d$
(1)	K	erg s <sup>-1</sup>	$M_{\odot}$	pc	K	erg s <sup>-1</sup>	$M_{\odot}$	pc
SDSSJ0000+1438	901±40	43.41±0.09	-2.01±0.12	-1.12±0.09	794±31	43.37±0.09	-1.07±0.11	-0.65±0.12
SDSSJ0027+0713	995±50	43.24±0.10	-2.35±0.14	-1.29±0.10	865±37	43.20±0.10	-1.39±0.13	-0.81±0.14
SDSSJ0045-0047	996±129	42.45±0.25	-3.14±0.34	-1.69±0.24	857±93	42.42±0.25	-2.20±0.31	-1.22±0.33
SDSSJ0103+1401	961±22	43.79±0.04	-1.74±0.06	-0.98±0.04	829±16	43.76±0.04	-0.81±0.05	-0.52±0.06
SDSSJ0120-0829	998±27	43.29±0.05	-2.31±0.07	-1.27±0.05	855±20	43.25±0.04	-1.37±0.06	-0.80±0.07

Table 2 continued



Table 2 (continued)

Name	$T_{bb}$	$\log L_{bb}$	$\log M_{bb}$	$\log R_{bb}$	$T_d$	$\log L_d$	$\log M_d$	$\log R_d$
	K	erg s <sup>-1</sup>	$M_{\odot}$	pc	K	erg s <sup>-1</sup>	$M_{\odot}$	pc
(1)	(2)	(3)	(4)	(5)	(6)	(7)	(8)	(9)
SDSSJ0121+1405	727±29	43.25±0.11	-1.80±0.13	-1.01±0.10	657±24	43.20±0.11	-0.90±0.13	-0.56±0.14
SDSSJ0158-0052	999±93	43.50±0.18	-2.10±0.25	-1.16±0.17	862±68	43.46±0.18	-1.15±0.23	-0.68±0.24
SDSSJ0205+0004	936±60	43.60±0.14	-1.88±0.18	-1.06±0.13	815±45	43.57±0.14	-0.94±0.17	-0.59±0.18
SDSSJ0745+2655	879±48	43.65±0.11	-1.72±0.14	-0.98±0.10	775±36	43.61±0.10	-0.78±0.13	-0.51±0.14
SDSSJ0757+1908	954±48	43.19±0.11	-2.33±0.14	-1.28±0.10	832±35	43.16±0.11	-1.37±0.13	-0.80±0.14
SDSSJ0811+4054	1072±39	43.60±0.06	-2.13±0.09	-1.18±0.06	912±27	43.56±0.06	-1.17±0.08	-0.70±0.09
SDSSJ0814+2611	689±12	43.21±0.04	-1.75±0.05	-0.99±0.04	623±10	43.15±0.04	-0.86±0.05	-0.55±0.05
SDSSJ0814+5337	945±40	43.36±0.10	-2.14±0.12	-1.18±0.09	828±30	43.33±0.09	-1.18±0.11	-0.70±0.12
SDSSJ0835+4935	864±47	43.12±0.09	-2.22±0.13	-1.23±0.10	757±35	43.08±0.09	-1.30±0.12	-0.77±0.13
SDSSJ0837+4143	880±47	43.34±0.12	-2.04±0.16	-1.13±0.11	775±36	43.31±0.12	-1.10±0.15	-0.66±0.16
SDSSJ0841+0526	1041±39	43.65±0.07	-2.02±0.10	-1.13±0.07	901±29	43.61±0.07	-1.04±0.09	-0.64±0.10
SDSSJ0842+2357	1192±50	42.86±0.06	-3.05±0.10	-1.64±0.07	994±33	42.82±0.06	-2.08±0.08	-1.15±0.09
SDSSJ0847+5142	729±33	43.04±0.10	-2.01±0.13	-1.12±0.09	657±26	42.99±0.10	-1.11±0.12	-0.67±0.13
SDSSJ0854+1113	1146±38	43.95±0.06	-1.88±0.08	-1.06±0.06	979±27	43.92±0.05	-0.87±0.07	-0.55±0.08
SDSSJ0858+4121	560±22	42.69±0.13	-1.91±0.15	-1.07±0.10	516±19	42.62±0.13	-1.06±0.14	-0.65±0.14
SDSSJ0859+0922	1010±61	43.90±0.13	-1.72±0.16	-0.97±0.12	878±45	43.86±0.12	-0.74±0.15	-0.48±0.16
SDSSJ0909+1920	729±40	43.34±0.14	-1.71±0.17	-0.97±0.12	657±32	43.29±0.14	-0.82±0.17	-0.53±0.17
SDSSJ0915+4814	1177±57	43.35±0.08	-2.53±0.12	-1.38±0.09	990±39	43.31±0.08	-1.54±0.11	-0.88±0.12
SDSSJ0931+6626	1012±34	42.77±0.07	-2.85±0.09	-1.54±0.06	872±24	42.73±0.06	-1.90±0.08	-1.06±0.09
SDSSJ0936+0615	2541±476	41.37±0.17	-5.86±0.37	-3.04±0.26	1657±179	41.16±0.13	-4.81±0.23	-2.51±0.34
SDSSJ0943+5958	725±16	42.51±0.06	-2.54±0.07	-1.38±0.05	652±12	42.46±0.06	-1.64±0.07	-0.93±0.07
SDSSJ0944+3105	955±41	42.85±0.08	-2.67±0.11	-1.45±0.08	824±30	42.82±0.07	-1.74±0.10	-0.99±0.11
SDSSJ0957+0207	1037±66	43.26±0.12	-2.40±0.17	-1.31±0.12	895±48	43.23±0.12	-1.42±0.15	-0.82±0.17
SDSSJ1001+1829	896±77	42.91±0.19	-2.50±0.24	-1.36±0.17	788±58	42.87±0.19	-1.56±0.23	-0.89±0.24
SDSSJ1002+4424	619±13	43.61±0.08	-1.15±0.09	-0.69±0.06	569±11	43.55±0.08	-0.31±0.08	-0.27±0.09
SDSSJ1003+0202	1159±97	43.36±0.15	-2.50±0.21	-1.36±0.15	981±67	43.32±0.15	-1.50±0.19	-0.86±0.21
SDSSJ1008+1549	985±73	43.52±0.16	-2.06±0.20	-1.14±0.14	856±54	43.48±0.15	-1.10±0.19	-0.66±0.20
SDSSJ1009+3436	1018±62	43.67±0.13	-1.96±0.17	-1.10±0.12	891±46	43.63±0.13	-0.97±0.16	-0.61±0.17
SDSSJ1009+2209	1115±63	43.61±0.11	-2.18±0.14	-1.21±0.10	953±44	43.57±0.10	-1.19±0.13	-0.72±0.14
SDSSJ1011+5348	992±59	43.97±0.13	-1.62±0.16	-0.92±0.12	873±45	43.93±0.12	-0.63±0.15	-0.43±0.16
SDSSJ1017+1224	1041±55	43.12±0.10	-2.55±0.14	-1.39±0.10	895±40	43.08±0.10	-1.58±0.12	-0.90±0.14
SDSSJ1020+2515	901±56	43.12±0.14	-2.30±0.18	-1.26±0.13	794±43	43.08±0.14	-1.35±0.17	-0.78±0.18
SDSSJ1029+2526	1772±192	44.14±0.15	-2.46±0.24	-1.34±0.17	1398±112	44.07±0.13	-1.30±0.19	-0.76±0.23
SDSSJ1029+4829	1140±96	44.04±0.13	-1.79±0.20	-1.01±0.14	983±70	44.00±0.13	-0.75±0.18	-0.49±0.19
SDSSJ1037+3912	738±34	43.19±0.13	-1.88±0.15	-1.05±0.11	664±27	43.14±0.13	-0.98±0.14	-0.60±0.15
SDSSJ1041+3412	1169±136	43.36±0.21	-2.51±0.29	-1.37±0.21	991±95	43.32±0.20	-1.51±0.26	-0.87±0.29
SDSSJ1043+2716	1035±63	43.44±0.11	-2.22±0.15	-1.23±0.11	894±46	43.40±0.10	-1.25±0.14	-0.75±0.15
SDSSJ1046+1655	1074±54	43.91±0.10	-1.82±0.13	-1.02±0.09	932±40	43.87±0.09	-0.81±0.12	-0.51±0.13
SDSSJ1051+2101	957±58	42.57±0.12	-2.96±0.16	-1.60±0.11	829±42	42.53±0.12	-2.02±0.15	-1.13±0.16
SDSSJ1053+5524	849±28	43.32±0.08	-2.00±0.10	-1.11±0.07	755±22	43.27±0.08	-1.07±0.09	-0.65±0.10
SDSSJ1058+5444	724±16	43.29±0.06	-1.75±0.07	-0.99±0.05	654±13	43.24±0.06	-0.86±0.07	-0.55±0.07
SDSSJ1105+5941	1156±32	43.33±0.04	-2.53±0.07	-1.38±0.05	964±22	43.28±0.04	-1.58±0.06	-0.90±0.07
SDSSJ1109+3708	881±25	42.74±0.06	-2.64±0.08	-1.44±0.05	768±19	42.70±0.06	-1.72±0.07	-0.98±0.07
SDSSJ1111+5923	1174±71	43.43±0.11	-2.45±0.15	-1.34±0.11	999±50	43.40±0.11	-1.43±0.14	-0.83±0.15
SDSSJ1114+4056	1114±36	43.73±0.05	-2.06±0.08	-1.14±0.05	954±25	43.69±0.05	-1.06±0.07	-0.64±0.07
SDSSJ1115+0544	858±167	43.49±0.45	-1.85±0.56	-1.04±0.40	757±128	43.45±0.44	-0.92±0.53	-0.57±0.56
SDSSJ1120+1933	1188±87	43.73±0.12	-2.17±0.18	-1.20±0.13	1002±60	43.69±0.12	-1.17±0.16	-0.70±0.18
SDSSJ1122+1433	1302±39	43.94±0.05	-2.12±0.07	-1.17±0.05	1091±26	43.90±0.05	-1.06±0.06	-0.64±0.07
SDSSJ1124+0455	697±17	43.25±0.07	-1.73±0.08	-0.98±0.06	629±13	43.20±0.07	-0.83±0.08	-0.53±0.08
SDSSJ1129+5131	580±6	42.99±0.03	-1.67±0.04	-0.95±0.03	530±5	42.93±0.03	-0.78±0.04	-0.50±0.04
SDSSJ1133+6701	994±74	43.00±0.14	-2.59±0.19	-1.41±0.13	853±53	42.96±0.13	-1.66±0.17	-0.94±0.18
SDSSJ1139+6134	747±20	43.35±0.08	-1.74±0.09	-0.99±0.06	673±16	43.30±0.07	-0.84±0.09	-0.54±0.09

Table 2 continued

Table 2 (continued)

Name	$T_{bb}$	$\log L_{bb}$	$\log M_{bb}$	$\log R_{bb}$	$T_d$	$\log L_d$	$\log M_d$	$\log R_d$
	K	erg s <sup>-1</sup>	$M_{\odot}$	pc	K	erg s <sup>-1</sup>	$M_{\odot}$	pc
(1)	(2)	(3)	(4)	(5)	(6)	(7)	(8)	(9)
SDSSJ149+5441	1078±92	43.05±0.16	-2.68±0.22	-1.45±0.15	915±64	43.02±0.15	-1.72±0.20	-0.97±0.21
SDSSJ152+4850	1115±80	43.82±0.12	-1.97±0.17	-1.10±0.12	954±57	43.78±0.12	-0.97±0.16	-0.60±0.17
SDSSJ153+4037	990±41	43.49±0.08	-2.10±0.11	-1.16±0.08	862±30	43.45±0.08	-1.13±0.10	-0.67±0.11
SDSSJ1200+0648	730±28	43.46±0.09	-1.60±0.12	-0.91±0.08	653±22	43.41±0.09	-0.70±0.11	-0.46±0.11
SDSSJ1201+3525	985±27	43.91±0.06	-1.66±0.07	-0.95±0.05	863±21	43.88±0.05	-0.68±0.07	-0.46±0.07
SDSSJ1203+5859	807±38	42.29±0.10	-2.94±0.13	-1.58±0.09	714±29	42.25±0.10	-2.02±0.13	-1.12±0.13
SDSSJ1208+3305	1087±80	43.73±0.14	-2.02±0.19	-1.12±0.14	949±60	43.69±0.14	-0.98±0.18	-0.60±0.19
SDSSJ1209+3202	1050±27	43.38±0.04	-2.31±0.06	-1.27±0.04	895±19	43.34±0.04	-1.36±0.06	-0.79±0.06
SDSSJ1211+4047	1243±113	44.24±0.18	-1.74±0.24	-0.98±0.17	1072±82	44.21±0.18	-0.63±0.22	-0.43±0.24
SDSSJ1214+1014	1016±161	43.58±0.33	-2.05±0.43	-1.14±0.31	882±119	43.55±0.33	-1.07±0.40	-0.65±0.43
SDSSJ1218+2951	877±48	43.64±0.13	-1.73±0.16	-0.98±0.11	776±37	43.60±0.12	-0.79±0.15	-0.51±0.16
SDSSJ1219+0516	964±60	43.29±0.12	-2.25±0.16	-1.24±0.12	836±44	43.25±0.12	-1.31±0.15	-0.77±0.16
SDSSJ1228+3617	1089±92	43.48±0.16	-2.27±0.22	-1.25±0.16	934±66	43.45±0.16	-1.28±0.20	-0.76±0.22
SDSSJ1238+0815	949±22	43.45±0.04	-2.06±0.06	-1.14±0.04	829±16	43.41±0.04	-1.11±0.06	-0.66±0.06
SDSSJ1242+2537	898±60	42.91±0.15	-2.51±0.19	-1.37±0.13	787±45	42.87±0.15	-1.57±0.18	-0.90±0.18
SDSSJ1245-0147	797±40	43.71±0.14	-1.50±0.16	-0.86±0.11	719±32	43.66±0.13	-0.58±0.16	-0.40±0.16
SDSSJ1303+2203	1259±101	43.16±0.13	-2.84±0.19	-1.54±0.13	1045±67	43.12±0.12	-1.85±0.16	-1.04±0.18
SDSSJ1305+3953	1060±41	43.16±0.07	-2.54±0.10	-1.39±0.07	905±29	43.12±0.07	-1.59±0.09	-0.91±0.10
SDSSJ1308+0429	982±45	42.78±0.09	-2.79±0.12	-1.51±0.08	845±33	42.74±0.09	-1.85±0.11	-1.04±0.11
SDSSJ1310+2518	1053±72	43.50±0.14	-2.19±0.18	-1.21±0.13	911±52	43.46±0.13	-1.20±0.17	-0.72±0.18
SDSSJ1315+0727	1167±50	43.55±0.07	-2.32±0.10	-1.28±0.07	982±34	43.51±0.07	-1.34±0.09	-0.79±0.10
SDSSJ1322+3301	911±23	43.40±0.06	-2.04±0.07	-1.14±0.05	801±17	43.36±0.05	-1.10±0.07	-0.67±0.07
SDSSJ1328+2752	1028±72	43.34±0.13	-2.31±0.18	-1.27±0.13	884±52	43.31±0.13	-1.35±0.16	-0.79±0.18
SDSSJ1329+2341	694±19	43.13±0.07	-1.83±0.09	-1.03±0.06	626±15	43.08±0.07	-0.94±0.09	-0.58±0.09
SDSSJ1332+2036	1001±26	43.86±0.05	-1.74±0.07	-0.99±0.05	867±19	43.82±0.05	-0.78±0.07	-0.51±0.07
SDSSJ1337+0035	1288±108	44.59±0.13	-1.45±0.20	-0.84±0.14	1098±76	44.55±0.12	-0.35±0.17	-0.29±0.19
SDSSJ1340+1842	945±59	42.79±0.12	-2.72±0.16	-1.47±0.12	823±44	42.75±0.12	-1.77±0.15	-1.00±0.16
SDSSJ1341-0049	1226±105	43.81±0.14	-2.14±0.21	-1.19±0.15	1036±73	43.77±0.14	-1.11±0.18	-0.68±0.20
SDSSJ1341+1516	831±25	43.33±0.07	-1.95±0.09	-1.09±0.06	739±20	43.28±0.07	-1.03±0.08	-0.63±0.09
SDSSJ1348+1559	1043±52	44.01±0.10	-1.67±0.13	-0.95±0.09	906±39	43.97±0.09	-0.67±0.12	-0.45±0.13
SDSSJ1352+0009	944±37	43.42±0.08	-2.08±0.11	-1.16±0.08	830±28	43.38±0.08	-1.12±0.10	-0.68±0.11
SDSSJ1402+3922	1177±45	43.63±0.06	-2.26±0.09	-1.24±0.07	984±30	43.59±0.06	-1.29±0.08	-0.76±0.09
SDSSJ1406+0628	861±17	43.37±0.04	-1.97±0.06	-1.10±0.04	759±13	43.33±0.04	-1.04±0.05	-0.64±0.06
SDSSJ1409+1057	662±17	43.17±0.07	-1.72±0.09	-0.97±0.06	600±14	43.11±0.07	-0.83±0.08	-0.53±0.09
SDSSJ1412+4114	1227±46	43.13±0.06	-2.83±0.09	-1.53±0.06	1025±30	43.09±0.06	-1.83±0.08	-1.03±0.09
SDSSJ1422+0609	1105±22	43.58±0.03	-2.20±0.05	-1.21±0.03	933±15	43.54±0.03	-1.24±0.04	-0.73±0.04
SDSSJ1424+6249	1188±50	43.35±0.06	-2.56±0.10	-1.39±0.07	999±34	43.31±0.06	-1.56±0.08	-0.89±0.09
SDSSJ1428-0231	940±101	42.34±0.22	-3.16±0.29	-1.69±0.20	815±75	42.30±0.21	-2.22±0.26	-1.22±0.28
SDSSJ1430+2303	1204±63	43.62±0.09	-2.31±0.13	-1.27±0.09	1005±42	43.57±0.08	-1.33±0.11	-0.78±0.12
SDSSJ1440+1758	927±55	42.80±0.13	-2.67±0.16	-1.45±0.12	812±41	42.76±0.12	-1.73±0.15	-0.98±0.16
SDSSJ1442+5558	1158±35	44.06±0.05	-1.79±0.07	-1.01±0.05	973±23	44.03±0.05	-0.82±0.06	-0.52±0.07
SDSSJ1447+4023	1202±46	43.80±0.07	-2.12±0.09	-1.18±0.07	1012±32	43.76±0.06	-1.12±0.08	-0.68±0.09
SDSSJ1448+1137	828±19	43.00±0.05	-2.28±0.06	-1.25±0.05	732±15	42.96±0.05	-1.36±0.06	-0.79±0.07
SDSSJ1504+0107	1140±37	44.20±0.05	-1.63±0.08	-0.93±0.06	969±26	44.16±0.05	-0.64±0.07	-0.44±0.08
SDSSJ1508+2602	657±22	42.97±0.10	-1.90±0.12	-1.07±0.08	597±18	42.91±0.10	-1.02±0.11	-0.63±0.11
SDSSJ1511+2214	848±33	43.40±0.09	-1.91±0.11	-1.07±0.08	752±26	43.36±0.09	-0.98±0.11	-0.61±0.11
SDSSJ1512+2809	761±19	43.12±0.06	-2.00±0.08	-1.12±0.05	683±15	43.07±0.06	-1.10±0.07	-0.67±0.07
SDSSJ1513+3111	1147±31	43.32±0.05	-2.52±0.07	-1.37±0.05	964±21	43.28±0.05	-1.55±0.06	-0.89±0.07
SDSSJ1524+5314	1202±84	42.92±0.11	-3.00±0.16	-1.61±0.11	1005±57	42.88±0.10	-2.02±0.14	-1.12±0.15
SDSSJ1531+3724	1026±93	42.19±0.17	-3.46±0.23	-1.84±0.16	874±66	42.15±0.16	-2.52±0.21	-1.37±0.22
SDSSJ1533+2729	959±84	43.48±0.17	-2.05±0.23	-1.14±0.16	831±62	43.44±0.16	-1.11±0.21	-0.67±0.22
SDSSJ1537+5814	1102±128	43.71±0.20	-2.06±0.28	-1.14±0.20	937±90	43.68±0.19	-1.08±0.25	-0.65±0.27

Table 2 continued

**Table 2** (*continued*)

Name	$T_{\text{bb}}$	$\log L_{\text{bb}}$	$\log M_{\text{bb}}$	$\log R_{\text{bb}}$	$T_{\text{d}}$	$\log L_{\text{d}}$	$\log M_{\text{d}}$	$\log R_{\text{d}}$
	K	$\text{erg s}^{-1}$	$M_{\odot}$	pc	K	$\text{erg s}^{-1}$	$M_{\odot}$	pc
(1)	(2)	(3)	(4)	(5)	(6)	(7)	(8)	(9)
SDSSJ1540+0054	894±82	40.78±0.18	-4.63±0.24	-2.43±0.17	776±60	40.74±0.18	-3.71±0.23	-1.97±0.24
SDSSJ1541+0718	933±77	43.29±0.19	-2.19±0.23	-1.21±0.17	821±59	43.25±0.18	-1.23±0.22	-0.73±0.23
SDSSJ1548+2208	998±32	43.25±0.06	-2.35±0.08	-1.29±0.06	854±23	43.21±0.06	-1.42±0.07	-0.82±0.08
SDSSJ1549+3327	1053±54	43.37±0.09	-2.33±0.13	-1.28±0.09	901±39	43.33±0.09	-1.36±0.12	-0.79±0.13
SDSSJ1554+5255	868±6	43.16±0.02	-2.19±0.02	-1.21±0.01	763±4	43.12±0.01	-1.27±0.02	-0.75±0.02
SDSSJ1554+1636	1026±116	40.69±0.20	-4.95±0.28	-2.59±0.20	871±81	40.65±0.20	-4.03±0.25	-2.13±0.27
SDSSJ1554+3629	1207±169	44.01±0.27	-1.92±0.36	-1.07±0.26	1032±120	43.97±0.26	-0.86±0.33	-0.54±0.36
SDSSJ1555+2120	741±17	43.19±0.06	-1.89±0.07	-1.06±0.05	664±14	43.14±0.06	-0.99±0.07	-0.61±0.07
SDSSJ1556+4513	1009±76	43.64±0.15	-1.98±0.20	-1.10±0.14	881±56	43.60±0.14	-0.99±0.18	-0.61±0.19
SDSSJ1557+2727	617±5	43.05±0.03	-1.72±0.03	-0.97±0.02	561±4	42.99±0.02	-0.83±0.03	-0.53±0.03
SDSSJ1600+4612	929±27	43.63±0.07	-1.85±0.09	-1.04±0.06	821±21	43.59±0.07	-0.88±0.08	-0.55±0.09
SDSSJ1612+1416	708±13	42.72±0.05	-2.28±0.06	-1.26±0.04	638±11	42.67±0.05	-1.39±0.06	-0.81±0.06
SDSSJ1620+2407	1349±99	43.32±0.10	-2.80±0.17	-1.51±0.12	1096±62	43.27±0.10	-1.81±0.14	-1.01±0.16
SDSSJ1628+4810	778±26	43.01±0.09	-2.16±0.11	-1.19±0.07	698±21	42.96±0.09	-1.25±0.10	-0.74±0.10
SDSSJ1632+4416	1235±76	43.17±0.10	-2.80±0.15	-1.52±0.11	808±13	42.63±0.04	-1.88±0.05	-1.06±0.14
SDSSJ1647+3843	1036±51	43.25±0.10	-2.42±0.13	-1.32±0.09	1027±51	43.12±0.10	-1.82±0.13	-1.02±0.13
SDSSJ1657+2345	842±33	43.93±0.09	-1.37±0.11	-0.80±0.08	749±26	43.83±0.08	-0.53±0.10	-0.38±0.11
SDSSJ1659+2049	633±8	43.10±0.04	-1.71±0.05	-0.97±0.03	708±10	42.80±0.04	-1.46±0.05	-0.85±0.05
SDSSJ2115-0011	1206±94	43.67±0.14	-2.25±0.19	-1.24±0.14	1333±130	43.54±0.16	-1.75±0.23	-0.99±0.20
SDSSJ2141-0857	912±41	43.01±0.09	-2.43±0.12	-1.33±0.09	794±31	42.89±0.09	-1.56±0.11	-0.90±0.12
SDSSJ2146+1041	1818±466	43.38±0.28	-3.26±0.52	-1.74±0.37	848±52	43.26±0.15	-1.28±0.18	-0.75±0.46
SDSSJ2150-0106	1255±205	43.35±0.24	-2.64±0.37	-1.44±0.26	1043±135	43.24±0.22	-1.73±0.32	-0.99±0.36
SDSSJ2156+0041	692±12	42.74±0.04	-2.22±0.05	-1.22±0.04	709±13	42.45±0.05	-1.80±0.06	-1.01±0.06
SDSSJ2203+1124	1024±70	43.92±0.15	-1.73±0.19	-0.98±0.13	909±54	43.85±0.15	-0.79±0.18	-0.51±0.18
SDSSJ2215-0107	801±27	42.79±0.08	-2.43±0.10	-1.33±0.07	789±24	42.69±0.07	-1.77±0.09	-1.00±0.10
SDSSJ2310+2220	883±29	42.90±0.07	-2.49±0.09	-1.36±0.07	796±23	42.68±0.07	-1.79±0.09	-1.01±0.09
SDSSJ2312+1335	985±49	43.33±0.10	-2.24±0.13	-1.24±0.09	853±36	43.17±0.10	-1.38±0.12	-0.81±0.13
SDSSJ2324+1542	1202±70	43.70±0.10	-2.22±0.15	-1.22±0.10	1168±78	43.54±0.12	-1.58±0.17	-0.90±0.15

NOTE— (1): Object name. (2)-(4): Dust temperature, luminosity and mass fitted with blackbody model at the epoch of W2 luminosity maximum. The dust mass is in unit of solar mass. (5): The distance of the dust to the central heating source assuming spherically symmetric distribution and covering factor 1. (6)-(9): similar to (2)-(5) but with the dust absorption coefficient considered.

**Table 3.** Optical counterparts

Galaxy	Transient	Date	Offset	AT Designation	Classification
(1)	(2)	(3)	(4)	(5)	(6)
SDSSJ0045-0047	PS16dsp	2016-08-03	0.39	AT2016ezq	...
SDSSJ0158-0052	PS16dtm	2016-08-12	0.16	SN2016ezh	TDE
SDSSJ0841+0526	ATLAS17nvk	2017-11-15	$< 0.5^a$	AT2017jdg	...
SDSSJ0854+1113	GNT	2016-09-26	$< 0.5^a$	...	...
SDSSJ0915+4814	ZTF18aaidlyq	2018-11-03	0.13	AT2018ivp	Turn-on AGN
SDSSJ0936+0615	ASASSN-18xl	2018-10-09	2.93	SN2018hfm	SNe
SDSSJ1133+6701	ZTF18aasuray	2018-05-10	0.09	AT2018cdp	Turn-on AGN
SDSSJ1332+2036	CRTS_OBC	2015-03-29	...	...	...
SDSSJ1531+3724	ASASSN-17jq	2017-07-25	1.93	AT2017fra	SNe
SDSSJ1533+2729	ATLAS18mtv	2017-12-30	0.27	AT2017kav	...
SDSSJ1540+0054	ASASSN-16eh	2016-04-10	1.20	SN2016blz	SNe
SDSSJ1554+1636	ASASSN-15bd	2015-01-17	1.00	...	SNe
SDSSJ1554+3629	iPTF16bco	2016-06-01	0.44	...	Turn-on AGN
SDSSJ1620+2407	ATLAS17jrp	2017-08-03	0.00	AT2017gge	TDE candidate
SDSSJ1647+3843	GNT	2017-06-10	$< 0.5^a$	...	...

NOTE— (1): SDSS abbreviated Name of the galaxy. (2): The transient named by the discovering surveys. (3): Optical discovery date. (4): Distance to the galactic center in unit of arcsec. (5): Designation on the transient name server. (6): The classified nature of the transients.

<sup>a</sup>The precise offset is unknown but should be  $< 0''.5$  because of the selection criteria of Gaia nuclear transient (Kostrzewa-Rutkowska et al. 2018)

**Table 4.** The properties of host galaxies and black hole

Name	$M_r$	g-r	$\sigma_*$	$\log M_*$	$\log \text{SFR}$	$\log M_{\text{BH}}$	Type
(1)	(2)	(3)	(4)	(5)	(6)	(7)	(8)
SDSSJ0000+1438	-21.54	0.89	192.	11.11	-0.13	8.23	Seyfert
SDSSJ0027+0713	-21.48	0.96	154.	11.05	0.89	7.68	Seyfert
SDSSJ0045-0047	-19.48	0.41	44.9	9.604	-0.10	6.00	StarForming
SDSSJ0103+1401	-21.39	0.71	94.2	10.73	0.94	6.47	StarForming
SDSSJ0120-0829	-20.83	0.79	115.	10.73	0.80	6.79	Seyfert(b)
SDSSJ0121+1405	-21.49	0.77	130.	10.91	0.49	7.26	StarForming
SDSSJ0158-0052	-19.49	0.61	45.4	10.15	-0.09	6.37	StarForming(b)
SDSSJ0205+0004	-20.44	0.71	112.	10.55	0.56	6.92	StarForming
SDSSJ0745+2655	-21.46	0.40	123.	10.18	1.60	7.22	Seyfert(b)
SDSSJ0757+1908	-21.19	0.71	131.	10.59	0.40	7.29	Composite
SDSSJ0811+4054	-20.37	0.65	120.	10.16	1.50	6.81	Seyfert(b)
SDSSJ0814+2611	-21.02	0.92	176.	10.78	0.32	8.01	StarForming
SDSSJ0814+5337	-21.51	0.71	165.	10.84	0.44	7.86	StarForming
SDSSJ0835+4935	-21.42	0.76	128.	10.77	-3.34	7.23	Composite
SDSSJ0837+4143	-21.48	0.92	167.	10.92	0.47	7.88	Composite
SDSSJ0841+0526	-22.36	0.91	145.	11.32	0.69	8.28	LINER(b)
SDSSJ0842+2357	-20.69	0.74	61.1	10.53	0.29	5.41	StarForming
SDSSJ0847+5142	-21.12	0.70	134.	10.67	0.46	7.35	StarForming
SDSSJ0854+1113	-22.82	0.95	281.	11.60	1.29	7.63	LINER(b)
SDSSJ0858+4121	-20.19	0.91	127.	10.46	-4.38	7.22	Composite
SDSSJ0859+0922	-21.94	0.60	66.1	10.88	0.79	5.60	StarForming
SDSSJ0909+1920	-20.65	0.79	101.	10.54	-0.87	6.66	Composite
SDSSJ0915+4814	-21.64	0.99	138.	10.85	-0.52	7.42	LINER
SDSSJ0931+6626	-20.82	1.06	147.	10.92	-4.06	7.56	LINER
SDSSJ0936+0615	-16.10	0.51	26.4	8.175	-1.67	4.57	StarForming
SDSSJ0943+5958	-20.07	0.88	97.4	10.44	-4.41	6.55	LINER
SDSSJ0944+3105	-22.03	0.67	147.	11.10	-0.09	7.58	Composite
SDSSJ0957+0207	-21.03	0.85	123.	10.73	0.23	7.14	Composite
SDSSJ1001+1829	-20.73	0.73	94.5	10.26	-0.17	6.48	StarForming
SDSSJ1002+4424	-22.43	0.93	223.	11.39	-3.48	8.58	LINER
SDSSJ1003+0202	-21.20	0.90	115.	10.75	0.06	6.96	Seyfert
SDSSJ1008+1549	-21.63	0.80	139.	11.04	0.92	7.44	Seyfert
SDSSJ1009+3436	-22.20	0.74	109.	11.00	1.30	6.84	Composite
SDSSJ1009+2209	-21.88	0.91	182.	11.24	0.62	7.97	Seyfert(b)
SDSSJ1011+5348	-22.36	1.08	246.	11.38	0.20	8.82	LINER
SDSSJ1017+1224	-20.49	0.77	120.	10.57	-0.04	7.07	Seyfert
SDSSJ1020+2515	-21.32	0.47	65.8	10.16	0.54	5.59	StarForming
SDSSJ1029+2526	-21.98	0.41	41.3	10.52	1.30	6.59	StarForming(b)

**Table 4** *continued*

Table 4 (continued)

Name	$M_r$	g-r	$\sigma_*$	$\log M_*$	$\log \text{SFR}$	$\log M_{\text{BH}}$	Type
(1)	(2)	(3)	(4)	(5)	(6)	(7)	(8)
SDSSJ1029+4829	-22.31	0.31	123.	10.68	1.67	7.47	Seyfert(b)
SDSSJ1037+3912	-20.58	0.72	81.6	10.50	0.31	6.12	StarForming
SDSSJ1041+3412	-21.54	0.72	129.	10.73	0.48	7.32	Composite(b)
SDSSJ1043+2716	-20.89	0.79	101.	10.37	-0.13	6.65	Composite
SDSSJ1046+1655	-22.44	0.92	220.	11.42	0.97	8.55	LINER
SDSSJ1051+2101	-20.12	0.86	104.	10.39	-0.16	6.71	Seyfert
SDSSJ1053+5524	-21.97	0.51	51.4	10.87	1.10	4.99	StarForming
SDSSJ1058+5444	-21.33	0.56	90.7	10.58	0.63	6.38	StarForming
SDSSJ1105+5941	-21.17	0.64	122.	10.80	0.66	7.03	Seyfert(b)
SDSSJ1109+3708	-20.84	0.75	150.	10.58	-4.15	7.62	LINER
SDSSJ1111+5923	-22.02	0.74	169.	10.79	0.21	7.91	Composite
SDSSJ1114+4056	-21.65	0.96	214.	11.33	0.66	8.10	Seyfert(b)
SDSSJ1115+0544	-20.70	0.98	125.	10.75	-1.90	7.18	LINER
SDSSJ1120+1933	-21.62	0.61	131.	10.76	1.14	7.28	Composite
SDSSJ1122+1433	-22.19	0.86	216.	11.33	1.47	7.90	Seyfert(b)
SDSSJ1124+0455	-21.27	0.68	94.4	10.27	0.78	6.48	Composite
SDSSJ1129+5131	-20.94	0.74	111.	10.74	0.45	6.89	Composite
SDSSJ1133+6701	-21.38	0.82	142.	10.91	-0.36	7.53	LINER(b)
SDSSJ1139+6134	-21.87	0.47	113.	10.81	1.00	6.94	StarForming
SDSSJ1149+5441	-20.96	0.75	101.	10.30	0.23	6.65	StarForming
SDSSJ1152+4850	-21.51	0.71	171.	10.46	0.89	7.94	Composite
SDSSJ1153+4037	-21.45	0.49	95.5	10.27	0.89	6.51	StarForming
SDSSJ1200+0648	-21.53	0.89	166.	11.12	0.96	7.87	Seyfert
SDSSJ1201+3525	-22.31	0.84	182.	11.23	0.56	8.09	Seyfert
SDSSJ1203+5859	-18.76	0.61	57.3	9.198	-0.63	5.26	StarForming
SDSSJ1208+3305	-21.86	1.02	261.	11.24	1.63	8.97	Seyfert
SDSSJ1209+3202	-21.21	0.82	148.	10.78	0.40	7.58	Seyfert
SDSSJ1211+4047	-22.06	1.07	175.	11.21	0.45	7.99	LINER
SDSSJ1214+1014	-21.39	0.60	44.7	10.69	0.55	7.09	Seyfert
SDSSJ1218+2951	-21.55	0.57	127.	10.61	0.56	7.22	Composite
SDSSJ1219+0516	-20.24	0.77	47.2	10.30	-0.06	6.70	Composite
SDSSJ1228+3617	-21.36	0.67	81.9	10.58	0.29	6.13	StarForming
SDSSJ1238+0815	-21.07	0.70	150.	10.36	0.67	7.62	Seyfert
SDSSJ1242+2537	-20.25	0.93	116.	10.49	-4.44	6.99	Composite
SDSSJ1245-0147	-22.34	0.61	127.	10.92	0.24	7.32	LINER
SDSSJ1303+2203	-21.42	0.92	171.	10.93	0.53	7.71	Seyfert
SDSSJ1305+3953	-20.72	0.93	163.	10.67	-3.28	7.82	LINER
SDSSJ1308+0429	-20.86	0.95	161.	10.76	-4.18	7.79	Seyfert
SDSSJ1310+2518	-21.58	0.71	149.	10.63	1.19	7.61	Composite
SDSSJ1315+0727	-21.86	0.85	154.	11.00	0.46	6.53	Composite(b)

Table 4 continued



**Table 4** (*continued*)

Name	$M_r$	g-r	$\sigma_*$	$\log M_*$	$\log \text{SFR}$	$\log M_{\text{BH}}$	Type
(1)	(2)	(3)	(4)	(5)	(6)	(7)	(8)
SDSSJ1322+3301	-21.63	0.82	123.	10.96	0.93	7.13	LINER
SDSSJ1328+2752	-21.11	0.88	174.	10.76	0.34	7.98	Seyfert
SDSSJ1329+2341	-20.54	0.83	105.	10.40	-0.29	6.74	Composite
SDSSJ1332+2036	-21.39	0.77	74.3	10.83	0.89	6.53	Composite(b)
SDSSJ1337+0035	-22.58	0.73	209.	11.33	1.89	8.43	Composite
SDSSJ1340+1842	-20.46	0.91	132.	10.57	-0.53	6.81	Seyfert(b)
SDSSJ1341-0049	-21.95	0.67	176.	10.77	1.21	7.70	Seyfert(b)
SDSSJ1341+1516	-21.65	0.76	145.	10.65	0.47	7.53	Composite
SDSSJ1348+1559	-21.72	0.95	246.	11.22	1.00	8.83	LINER
SDSSJ1352+0009	-22.17	0.73	124.	10.83	0.20	7.16	LINER
SDSSJ1402+3922	-20.76	0.64	128.	10.31	-0.26	6.57	Seyfert(b)
SDSSJ1406+0628	-21.42	0.74	139.	10.85	0.91	7.43	StarForming
SDSSJ1409+1057	-22.26	0.75	180.	10.74	-0.39	8.06	LINER
SDSSJ1412+4114	-21.50	0.94	165.	11.11	-3.84	7.85	Composite
SDSSJ1422+0609	-21.96	0.85	...	11.21	0.47	7.61	...
SDSSJ1424+6249	-21.79	0.90	182.	11.08	0.16	8.09	Composite
SDSSJ1428-0231	-18.68	0.83	98.8	9.532	-0.11	6.59	Composite(b)
SDSSJ1430+2303	-21.04	1.01	183.	11.15	0.28	7.91	Seyfert(b)
SDSSJ1440+1758	-20.65	0.79	79.1	10.43	-0.27	6.04	Composite
SDSSJ1442+5558	-21.80	0.73	174.	10.60	0.74	7.98	Composite
SDSSJ1447+4023	-21.53	0.91	163.	11.24	-0.36	7.82	LINER
SDSSJ1448+1137	-21.09	0.80	101.	10.57	0.09	6.97	StarForming
SDSSJ1504+0107	-22.15	0.86	181.	11.24	1.57	8.07	Seyfert
SDSSJ1508+2602	-20.73	0.67	69.0	10.05	0.37	5.71	Composite
SDSSJ1511+2214	-21.45	1.02	225.	11.16	0.07	8.61	Seyfert
SDSSJ1512+2809	-21.39	0.93	152.	11.09	-3.89	7.65	LINER
SDSSJ1513+3111	-21.22	0.69	103.	10.63	-0.15	6.70	Composite
SDSSJ1524+5314	-20.08	0.60	78.0	10.38	0.11	6.01	StarForming
SDSSJ1531+3724	-16.99	0.43	23.9	8.375	-0.91	4.77	StarForming
SDSSJ1533+2729	-21.37	0.95	196.	11.01	0.55	8.14	Seyfert(b)
SDSSJ1537+5814	-20.45	0.84	86.0	10.53	0.70	7.23	Seyfert(b)
SDSSJ1540+0054	-16.66	0.40	33.4	8.231	-1.80	4.63	StarForming
SDSSJ1541+0718	-21.34	0.65	140.	10.81	0.63	7.45	StarForming
SDSSJ1548+2208	-19.01	0.93	73.7	9.976	-1.39	5.87	Composite
SDSSJ1549+3327	-20.12	0.58	64.8	9.796	-0.05	5.56	StarForming
SDSSJ1554+5255	-20.92	0.72	111.	10.50	-0.23	6.89	Composite
SDSSJ1554+1636	-15.98	0.42	79.8	7.946	-1.50	4.34	StarForming
SDSSJ1554+3629	-22.04	0.81	182.	11.13	0.83	8.08	LINER
SDSSJ1555+2120	-20.10	1.27	135.	10.88	-3.09	7.35	Composite
SDSSJ1556+4513	-21.04	0.75	170.	10.88	1.15	7.92	Seyfert

**Table 4** *continued*

**Table 4** (*continued*)

Name	$M_r$	g-r	$\sigma_*$	$\log M_*$	$\log \text{SFR}$	$\log M_{\text{BH}}$	Type
(1)	(2)	(3)	(4)	(5)	(6)	(7)	(8)
SDSSJ1557+2727	-20.43	0.94	111.	10.36	0.60	6.89	Composite
SDSSJ1600+4612	-22.30	0.77	161.	11.16	-0.67	7.80	StarForming
SDSSJ1612+1416	-20.53	0.87	123.	10.60	0.06	7.14	Composite
SDSSJ1620+2407	-20.76	0.70	102.	10.04	-1.02	6.67	StarForming
SDSSJ1628+4810	-21.25	0.48	61.4	10.11	0.70	5.43	StarForming
SDSSJ1632+4416	-20.51	0.88	158.	10.59	-4.26	7.74	LINER
SDSSJ1647+3843	-20.28	0.62	63.2	10.47	0.21	5.49	StarForming
SDSSJ1657+2345	-19.30	0.68	48.7	9.515	0.15	5.91	Seyfert
SDSSJ1659+2049	-21.67	0.87	148.	10.80	-0.02	7.58	Seyfert
SDSSJ2115-0011	-21.66	1.01	178.	11.17	1.41	7.48	Seyfert(b)
SDSSJ2141-0857	-20.50	0.79	106.	10.50	-0.41	6.77	Seyfert
SDSSJ2146+1041	-21.80	0.54	121.	10.55	0.80	7.09	StarForming
SDSSJ2150-0106	-18.97	1.00	70.3	10.05	-0.64	5.76	Seyfert
SDSSJ2156+0041	-20.75	0.87	114.	10.59	0.27	6.59	Seyfert(b)
SDSSJ2203+1124	-21.71	0.98	152.	10.74	-0.19	7.64	Composite
SDSSJ2215-0107	-21.40	1.01	107.	11.02	-0.10	6.79	Composite
SDSSJ2310+2220	-20.65	1.09	127.	10.89	0.57	7.22	Seyfert
SDSSJ2312+1335	-21.43	0.90	172.	10.91	0.77	7.95	Composite
SDSSJ2324+1542	-21.36	0.83	140.	10.94	0.42	7.83	Composite(b)

NOTE— (1): SDSS name. (2)-(3): SDSS  $r$ -band absolute magnitude and  $g-r$  color after  $k$ -correction to 0.1 . (4): Stellar velocity dispersion. (5): Stellar mass. (6): Estimated BH mass. (7): Classification in the BPT-diagram with suffix '(b)' highlighting robust broad  $\text{H}\alpha$  detection. (8): The logarithmic star formation rate in unit of  $M_{\odot}/\text{yr}$  (see §6.2).

**Table 5.** Radio properties of FIRST-detected objects

Name	Type	$F_{1.4}$	$\log L_{1.4}$	$\log \text{SFR}$	$F'_{1.4}$	$F'_{1.4}/F_{1.4}$	$R$	Class
(1)	(2)	(3)	(4)	(5)	(6)	(7)	(8)	(9)
SDSSJ0120-0829	Seyfert(b)	3.68	22.00	0.80	8.00	0.46	12	SF
SDSSJ0205+0004	StarForming	0.75	22.02	0.56	0.76	0.98	...	SF
SDSSJ0745+2655	Seyfert(b)	3.09	23.01	1.60	7.97	0.39	3	SF
SDSSJ0811+4054	Seyfert(b)	1.64	22.24	1.50	18.02	0.09	10	SF
SDSSJ1046+1655	LINER	69.72	24.91	0.97	0.32	216	29226	Jet
SDSSJ1105+5941	Seyfert(b)	5.96	22.19	0.66	5.62	1.06	12	w.Jet
SDSSJ1114+4056	Seyfert(b)	1.28	22.89	0.66	0.24	5.30	26	w.Jet
SDSSJ1129+5131	Composite	5.01	22.09	0.45	3.06	1.64	...	SF
SDSSJ1200+0648	Seyfert	5.18	22.19	0.96	12.16	0.43	15	SF
SDSSJ1211+4047	LINER	12.34	24.66	0.45	0.02	599	27722	Jet
SDSSJ1303+2203	Seyfert	1.76	22.60	0.53	0.43	4.12	19	w.Jet
SDSSJ1310+2518	Composite	1.83	23.09	1.19	1.09	1.69	...	SF
SDSSJ1328+2752	Seyfert	3.09	22.80	0.34	0.27	11.46	26	w.Jet
SDSSJ1337+0035	Composite	127.25	25.53	1.89	2.41	53	27566	Jet
SDSSJ1348+1559	LINER	17.46	24.19	1.00	0.46	38	3952	Jet
SDSSJ1406+0628	StarForming	2.55	22.65	0.91	1.80	1.42	...	SF
SDSSJ1430+2303	Seyfert(b)	1.63	22.41	0.28	0.28	5.77	13	w.Jet
SDSSJ1442+5558	Composite	1.03	22.16	0.74	1.31	0.78	...	SF
SDSSJ1504+0107	Seyfert	1.31	22.74	1.57	5.72	0.23	30	SF
SDSSJ1533+2729	Seyfert(b)	3.04	22.57	0.55	0.83	3.66	11	w.Jet
SDSSJ1557+2727	Composite	7.72	22.24	0.60	5.34	1.44	...	SF
SDSSJ2156+0041	Seyfert(b)	1.19	21.91	0.27	0.65	1.84	8	w.Jet

NOTE— (1): Name. (2): BPT type listed in Table 4. (3): Radio flux at 1.4 GHz in unit of mJy. (4): The logarithmic radio luminosity at 1.4 GHz in unit of  $\text{W Hz}^{-1}$  after k-correction. (5): SFR estimated from SDSS+WISE SED fitting or W4 flux. (6): Radio flux derived from SFR. (7): The ratio between the observed radio flux and the predicted one from star formation. (8): The radio-loudness parameter defined as the ratio of the monochromatic flux between 6 cm (5 GHz) and AGN continuum at 4400 Å ( $f_{\nu, 6\text{cm}}/f_{\nu, 4400}$ ). (9): The main origin of radio emission. 'SF': star formation. 'Jet': undisputed intense jet emission. 'w.Jet': jet likely contribute since the observed radio flux is higher than SFR prediction, but the radio power should be much weaker than 'Jet' as  $R$  is not very high ( $<30$ ).